Geothermics 130 (2025) 103323

Contents lists available at ScienceDirect

Geothermics

journal homepage: www.elsevier.com/locate/geothermics

Assessment of geothermal waters in Yunnan, China: Distribution, quality and driving factors

Zhaojun Zeng [a], Li Yang [c], Yueju Cui [a,*], Xiaocheng Zhou [a,b,*], Miao He [a], Yuwen Wang [a], Yucong Yan [a], Bingyu Yao [b], Xiaojing Hu [c], Weiye Shao [c], Jian Li [c], Hong Fu [c]

[a] United Laboratory of High-Pressure Physics and Earthquake Science, Institute of Earthquake Forecasting, China Earthquake Administration, Beijing, 100036, PR China
[b] School of Earth Sciences and Resources, China University of Geosciences, Beijing, 100083, PR China
[c] Yunnan Earthquake Agency, Kunming, 650224, PR China

ARTICLE INFO

Keywords:
Self-Organizing Map
Yunnan province
Geothermal water
Water quality
Health risk assessment

ABSTRACT

Geothermal energy is a vital renewable resource widely used for various applications, including drinking water, domestic supply, irrigation, and industrial purposes. However, the utilization of geothermal water for drinking can expose individuals to toxic elements, particularly arsenic, which poses significant health risks. Despite the growing interest in geothermal water, there has been a lack of systematic analysis regarding the spatial variability of its quality and health risk. This study aims to address this gap by evaluating the spatial variability of the water quality characteristics and health risks in Yunnan Province using a combination of hydrochemical and isotopic methods, Principal Component Analysis (PCA), Self-Organizing Maps (SOM) and integrated tools such as Water Quality Index (WQI) and Human Health Risk Assessment (HHRA). According to this study, atmospheric precipitation serves as the primary recharge source with Na-HCO_3, Ca-HCO_3, Na-Cl and Ca-Cl as the dominant geothermal water hydrochemical in Yunnan Province. While most samples exhibit good water quality, those from the northwestern regions (e.g., Lijiang, Lincang, Kunming, Baoshan, Jinghong, Pu'er, and Dali) show poorer water quality and significant health risks. PCA analysis reveals that the spatial variability of geothermal water quality is largely influenced by deep hydrological cycles and magma-tectonic interactions, resulting in arsenic enrichment in high-risk areas. This study addresses the research gap regarding the spatial variability of geothermal water quality and health risk assessment in Yunnan Province and provides a scientific foundation for sustainable development and management.

1. Introduction

Since the 20th century, the increasing demand for energy and materials has elevated resource development to a global priority. Geothermal energy, known for its sustainability and low environmental impact, has garnered significant attention (Abbasnia et al., 2018; Zhang et al., 2020a; Wei et al., 2022). Geothermal water serves as a vital resource for sustaining livelihoods, maintaining ecological balance and preserving biodiversity (Cacciapuoti et al., 2020; Tiwari et al., 2021; Sun et al., 2023; Zhang et al., 2023; Wang et al., 2024). Extensive research has demonstrated its widespread use in medical, recreational, and agricultural applications (Tong et al., 2000; Fagundo-Castillo et al., 2008; Tao et al., 2023). For example, hot springs have been recognized for their therapeutic benefits. The therapeutic properties of hot springs have stimulated the rapid growth of spa tourism, further driving the demand for geothermal resources. However, improper exploitation of geothermal water can pose significant risks to human health (Lee et al., 2019; Hakimi et al., 2021; Shen et al., 2023; Zhang et al., 2024; Yang et al., 2024). Therefore, a deeper understanding of the water quality and chemical characteristics of geothermal water is crucial to ensuring its sustainable use and protection.

Hot springs, as a form of geothermal energy, serve as key indicators of the deep geothermal water cycle and water chemistry (Luo et al., 2023; Sun et al., 2023; He et al., 2024). The formation and movement of geothermal waters are fundamentally controlled by structural geology. In particular, the tectonic features including fault systems and magmatic activity directly influence the chemical composition and spatial distribution of geothermal water (Hosono et al., 2018; Sato et al., 2020; Bao

* Corresponding authors at: United Laboratory of High-Pressure Physics and Earthquake Science, Institute of Earthquake Forecasting, China Earthquake Administration, Beijing, 100036, PR China.
E-mail addresses: cehuicuiyueju@126.com (Y. Cui), zhouxiaocheng188@163.com (X. Zhou).

https://doi.org/10.1016/j.geothermics.2025.103323
Received 2 September 2024; Received in revised form 26 February 2025; Accepted 12 March 2025
Available online 16 March 2025

et al., 2023; Chen and Liu, 2023; Xie et al., 2024). Extensive research has established the relationship between geothermal water and geological formations, including the correlation between hot spring distribution and seismic activity (Andrén et al., 2016; Li et al., 2019a; Zhang et al., 2020b). Geochemical modeling is extensively applied to model the hydrochemical characteristics of geothermal systems, enhancing our understanding of the coupling mechanisms between water quality evolution and the groundwater cycling (Luo et al., 2023; Tian et al., 2023; Yan et al., 2024). Additionally, stable isotope techniques have been widely employed to trace the sources and circulation pathways of geothermal waters, yielding critical constraints on their genetic mechanisms (Shi et al., 2020; Zhang et al., 2020c; Scorzini et al., 2023).

High-temperature geothermal resources are ubiquitously distributed across Yunnan Province (Liu et al., 2015; Guo et al., 2017,2021; Wang et al., 2020). A substantial body of research has investigated geothermal water have been conducted in Yunnan, primarily concentrating on geothermal formation mechanisms, tectonic interactions with hot springs, seismic anomaly identification and fluid circulation modeling (Li et al., 2021, 2022; Wang et al., 2022; Zhou et al., 2022; Luo et al., 2023; Ouyang et al., 2023; Li et al., 2024; He et al., 2024; Zhou et al., 2024). Previous studies have demonstrated that Yunnan's unique geological setting, combined with its intense faulting activity, creates favorable conditions for the formation and flow of geothermal water (Zhang et al., 2008; Wu et al., 2010; Liu et al., 2015; Zhang et al., 2020a; Guo et al., 2021; Lin et al., 2021; Wu et al., 2021; Li et al., 2022; Tao et al., 2023; Yang et al., 2024). The prevailing hypothesis suggests that atmospheric precipitation infiltrates the subsurface, where it is heated by a thermal source, and subsequently circulates along faults and fractures towards the surface, eventually contributing to hot spring recharge. Traditionally, hydrogeochemical characteristics have been analyzed using classical methods such as Piper diagrams, the Na-K-Mg ternary diagram, factor analysis (FA), discriminant analysis (DA), and cluster analysis (CA). However, these conventional approaches are often insufficient to reveal the intrinsic relationships between hydrochemical data (Hayton et al., 2004; Devic et al., 2014; Zhang et al., 2018; Li et al., 2019b; Coyte et al., 2020; Tiwari et al., 2021; Zhong et al., 2022). Water chemistry evolution typically involves multiple processes that can alter the level and distribution of variability. Moreover, numerous traditional methods are not capable of uncovering the multivariate nonlinear couplings.

Self-Organizing Maps (SOM), a specialized class of artificial neural networks, projects complex high-dimensional datasets through topological preservation. As a result, SOM has emerged as a pivotal tool for groundwater systems, particularly in assessing water quality, chemical composition and contamination (Li et al., 2018; Kim et al., 2020; Hakimi et al., 2021; Yotova et al., 2021; Samadi, 2022; Mia et al., 2023; Yang et al., 2023). For example, SOM has been applied to elucidate salinization mechanisms in groundwater in northern Germany's mining regions (Haselbeck et al., 2019) and to establish conceptual models to discriminate deep hot groundwater in South Korea (Kim et al., 2020). It has also been used in conjunction with the Water Quality Index (WQI) for surface water quality assessment in the Mesta River Basin, Bulgaria (Yotova et al., 2021). Moreover, SOM combined with Artificial Intelligence (EAI) and the Entropy Water Quality Index (EWQI) has been demonstrated exceptional efficacy in reconstructing the evolution of water chemistry in the Haor region of northeastern Bangladesh (Mia et al., 2023). In China, SOM has provided critical insights into the hydrochemistry of groundwater in various regions, including Panyang Lake in Hunan Province (Mao et al., 2021). It has also been used to understand the hydrochemical evolution of the Shengli Canal Irrigation District in northern Henan Province (Liu et al., 2023) and the spatiotemporal patterns of groundwater salinization of south-central Fujian Province (Li et al., 2018).

This study synergizes the SOM and K-means (KM) clustering methods to analyze the distribution of major ions, hydrogen and oxygen isotope compositions, and trace elements in the geothermal waters of Yunnan Province, to systematically investigate the spatial variations of these waters and their genesis. It builds on previous data (Li et al., 2021, 2022; Wang et al., 2022; Zhou et al., 2022; Luo et al., 2023; Ouyang et al., 2023; Li et al., 2024; He et al., 2024; Zhou et al., 2024), which have primarily centered on major ion geochemistry to reveal hydrochemical types and their genesis, but have paid limited attention to trace elements and water quality. By leveraging these data, this study provides the first comprehensive analysis of geothermal water quality in Yunnan Province, addressing a key gap in existing research and addressing critical knowledge gaps in geothermal water assessment. Specifically, this study emphasizes the role of trace elements, exploring the spatial distribution patterns of water quality and hydrogeochemical characteristics to gain deeper insights into the groundwater resources of the region. The findings provide to a deeper understanding of Yunnan's groundwater resources and provide a scientific foundation for the sustainable development and management of these resources. This study pursues three key objectives: 1) to classify the geothermal waters in the study area using SOM-K-means (SOM-KM) clustering, and to determine the origin and evolution of geothermal waters within each cluster; 2) to uncover spatial variations in water quality by comprehensively evaluating the water quality characteristics and health risks of Yunnan's geothermal waters in the context of the region's geological conditions; and 3) to delineate hydrochemical facies across distinct clusters and explore their underlying causes. Collectively, the findings provide a solid scientific basis for the sustainable development and management of geothermal water resources in Yunnan Province, offering valuable insights for similar regions.

2. Materials and methods

2.1. Study area

Yunnan Province, located in southwestern China (97°31′39″ to 106°11′47″E, 21°08′32″ to 29°19′08″N), spans approximately 394,000 km^2 (Chen et al., 2015; Liang et al., 2022). It is situated at the dynamic tectonic convergence zone where the Indian plate colliding with the Eurasian plate, contributing to the southeastward extrusion of the Tibetan Plateau. This results in diverse topography, with altitudes ranging from north to south, and the region experiencing dual influence from the South Asian and East Asian monsoons. The average annual temperature ranges from 15 °C to 22 °C, with precipitation varying between 1000 mm and 3000 mm (Bai, 2008; Liang et al., 2022).

Yunnan displays a complex geological architecture, with a complete stratigraphic succession spanning Paleoproterozoic to Quaternary periods. The lithology predominantly consists of marine carbonate rocks, interbedded with clastic sequences. It also is characterized by intense magmatic-metamorphic processes. Paleozoic carbonate rocks, such as dolomite and marl, are prevalent in the eastern part of the province, while volcanic rocks, primarily of Hercynian affinity, are widespread. The magnesian ultramafic rocks with ironstone mineralization are occur as tectonically emplaced units within the Tengchong-Sanjiang orogenic belt, with metamorphic rocks being extensively distributed across the province (Chen et al., 2015; Liang et al., 2022).

Yunnan is structurally segmented into three major tectonic units: the Tengchong-Sanjiang orogenic system, the Yangzi Block and the South China Block. The region is also crosscut by a network of neotectonic fault systems, including Xiaojiang Fault (XJF), Chuxiong-Jianshui Fault (CJF), Red River Fault (RRF), Langcang Gengma Fault (LGF), Lijiang Xiaojinhe Fault (LXF), Nanting River Fault (NTF) and Wuliangshan Fault (WLSF). These fault systems exert primary control on the regional geomorphological evolution, hydrology, geothermal activity, volcanism, and seismicity (Bai, 2008; Chen et al., 2015).

Yunnan's complex tectonic framework exerts fundamental control over the region's hydrogeological architecture (Chen et al., 2015; Guan, 2018). It is drained by six principal drainage systems: the Jinsha, Lancang, Nanpan, Nujiang, Dulongjiang, and Yuanjiang. Most of these

rivers originate from the Tibetan Plateau and flow southeastward through the Hengduan Mountains, ultimately discharging into the Pacific and Indian Oceans. These fault systems govern groundwater recharge mechanisms and modulate the deep-circulation recharge dynamics and spatial configuration of fracture-controlled aquifers.

Yunnan Province hosts a heterogeneous assemblage of aquifer systems, comprising loose rock aquifers, clastic rock fractured aquifers, carbonate rock aquifers, and metamorphic rock aquifers. The unconsolidated sedimentary aquifers predominantly occupy intermontane basins, with shallow water tables, good chemical quality, and moderate productivity. In contrast, clastic rock aquifers, dominate in orogenic belts and dissected uplands, exhibit deeper water tables and poorer chemical quality, yet exhibit higher productivity. Carbonate rock aquifers, particularly in the central and eastern parts of Yunnan, constitute critical water resources owing to their deeper storage and higher productivity, making them critical for regional water supply (Bai, 2008; Zhang, 2022).

In conclusion, the complex geology, tectonics and hydrology of Yunnan Province control the spatial distribution and hydrochemical characteristics of its groundwater resources. Notably, the region is home to more than 1000 hot springs, constituting over one-third of China's 2800 hot springs (Ren et al., 2018; Chen and Wang, 2021). Western Yunnan is notable for its numerous hot springs, high temperature and substantial natural flow (Fan et al., 2015; Zhou et al., 2022; Luo et al., 2023). The rapid development of hot spring tourism has significantly increased the demand for geothermal resources. Therefore, a comprehensive understanding of hot springs is essential to ensure their sustainable utilization in Yunnan.

2.2. Sampling and chemical analysis

Water sampling was conducted in Yunnan Province from March to May 2024. A total of 265 water samples were collected and including 37 samples were obtained from geothermal wells, 127 from cold water wells and 101 from hot springs. The remaining 146 samples were obtained from published datasets (Fig. 1) and additional data on arsenic (As) and mercury (Hg) concentrations were included for further analysis.

At each sampling site, triplicate subsamples were collected for the analysis of major ions, hydrogen and oxygen isotopes ($\delta^{18}O$ and δD), and trace elements. Prior to collection, each sample bottle was washed three times with the sample water. The water was then filtered through a 0.22 μm filter membrane and transferred into 100 mL polyethylene bottles. The bottles were sealed with parafilm to prevent contamination from the surrounding air. To preserve the stability of trace elements, 1–2 drops of 14M nitric acid were added to each sample and the pH was adjusted to below 2. The samples were then refrigerated. Water temperature (T) was measured at a standardized depth of 20 cm below the water surface using a calibrated Handheld Precision Digital Thermometer PR710A (±0.1 °C), after 5-minute stabilization in flowing water. And pH and conductivity were determined using a Thermo Scientific™ Orion Star™ A325 multiparameter meter (with an accuracy of 0.01).

The water samples were subjected to detailed hydrogeochemical analysis. The chemical composition, including cations (Mg^{2+}, Ca^{2+}, K^{+}, and Na^{+}) and anions (SO_4^{2-}, Br^{-}, Cl^{-}, and NO_3^{-}), was determined using ion chromatograph (Thermo Scientific Dionex AQUION IC) equipped with an AS40 automatic sampler, at the Key Laboratory of Earthquake Prediction of the China Seismological Bureau. The reproducibility of these measurements was ±2% and the detection limit was 0.01 mg/L. The HCO_3^{-} and CO_3^{2-} concentrations were analyzed using a ZDJ-100 potentiometric titration with 0.05 mol/L of HCl, employing 0.1 % methyl orange and 1% phenolphthalein as indicators, achieving a reproducibility of ±2 %. Trace elements were conducted in the same laboratory using an Agilent 8900 ICP-QQQ. The $\delta^{18}O$ and δD were determined using a Picarro L2140-I Liquid water and vapor isotope analyzer, with Vienna Standard Mean Ocean Water (V-SMOW) as the reference standard. The $\delta^{18}O$ and δD values were measured with accuracies of ±0.2 % and ±1 %, respectively.

$$ib(\%) = \frac{\sum cations - \sum anions}{0.5(\sum cations + \sum anions)} \times 100 \quad (1)$$

If the balance error between anions and cations is less than ±10%, the results for the major ions can be considered reliable for analyzing the hydrogeochemical characteristics (Woith et al. 2013).

2.3. Self-organizing map (SOM)

SOM is a robust neural network designed for unsupervised learning, which maps complex high-dimensional data onto a two-dimensional hexagonal grid of neurons, thereby enhancing the visibility of topological properties (Mao et al., 2021; Zhang et al., 2022). Typically, the formula $m = 5\sqrt{n}$ is used to estimate the number of neurons, where m

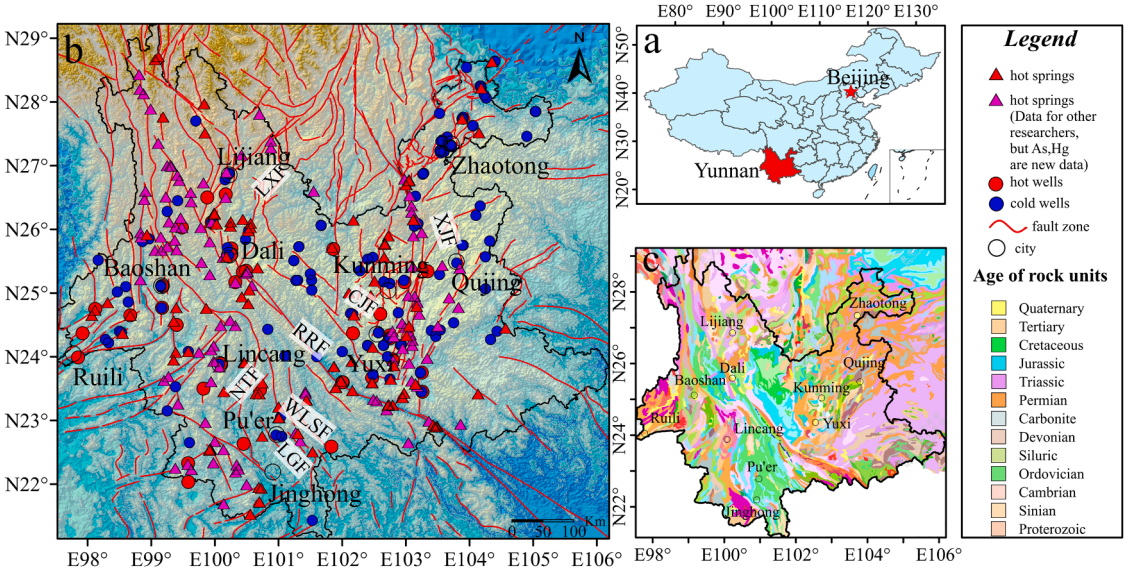

Fig. 1. (a) China Map indicating the location of Yunnan Province; (b) Map of the study area indicating the distribution of sample sites; (c) Map of the study area indicating the distribution of lithology.

represents the SOM neurons' number and *n* refers to the number of input samples (Nguyen et al., 2015). However, SOM lacks inherent capability to determine the optimal cluster number. To overcome this limitation, the KM algorithm is applied to SOM outputs to find the optimal clusters and classify water samples based on the minimal Davis-Bouldin index (DBI) (Zhang et al., 2023).

While it is not possible to objectively define the exact mapping units, the selection of mapping units can be assessed using quantization error (QE) and topographic error (TE). The ideal number of mapping units is identified at the local minimum of QE and TE (Astel et al., 2007; Tsakovski and Simeonov, 2011). SOM models are commonly constructed using MATLAB software, with selected element concentrations as the input dataset for both computation and visualization. This approach allows SOM to effectively interpret the distribution patterns within multivariate hydrochemical datasets, revealing correlations within and between sample groups (Shen et al., 2023).

2.4. Water quality index (WQI) and Human Health Risk Assessment (HHRA)

WQI and HHRA methods have been used to assess trace element water quality and potential health risks. This study uses the arithmetic WQI for its computational robustness under high-dimensional hydrochemical variability. Water quality assessment is complex, with parameter weighting schemes contingent on dataset characteristics, local environment, geology, and demands. Expert-based weighting frameworks incorporate domain-specific knowledge, reflecting regional realities and challenges. This method assigns weights based on researchers' experience, making it more adaptable and reliable in complex hydrogeological settings (Xiao et al., 2021; Krishan et al., 2023). The WQI was calculated by initially assigning a weight (*wi*) to each water quality parameter based on its relative importance to drinking water quality, as determined on a scale of 1 to 5 (Githaiga et al., 2021). The weight (W_i) of each parameter was subsequently calculated using the formula $W_i = \frac{wi}{\sum wi}$ (Njuguna et al., 2020). The water quality grade (q_i) for each parameter was computed by calculating the ratio of the parameter's concentration (C_i) to its maximum permissible limit (S_i) as specified by World Health Organization (WHO), and then multiplying by 100: $q_i = \frac{C_i}{S_i} \times 100$ (Krishan et al., 2023). The sub-index (SI_i) for each parameter was calculated using $SI_i = W_i \times q_i$, and the overall WQI was obtained by summing all sub-indices: $WQI = \sum_{i=1}^{N} SI_i$. The WQI categorizes water quality into five levels: unsuitable for drinking water (>300); very poor (200 to 300); fair (100 to 200); good (50 to 100) and excellent (<50) (Njuguna et al., 2020; Githaiga et al., 2021). Trace elements migrate into human systems predominantly via the body through ingestion of contaminated water and dermal touch. In this study, the HHRA employed the widely adopted US EPA method to assess health risks from these routes in adults and children. For HHRA, the exposure dose for ingestion (*ADDingestion*) and dermal contact (*ADDdermal*) was calculated using the formulas $ADDingestion = \frac{Cw \times IR \times EF \times ED}{BW \times AT}$ and $ADDdermal = \frac{Cw \times SA \times Kp \times EF \times ET \times ED \times CF}{BW \times AT}$. The hazard quotient (*HQ*) and hazard index (*HI*) were then determined using $HQ = \frac{ADD}{RfD}$ and $HI = \sum(\text{HQingestion} + \text{HQdermal})$. The HI classification criteria are as following: $HI < 0.1$, no cancer risk; $0.1 \leq HI < 1$, low noncancer risk; $1 \leq HI < 4$, moderate noncancer risk; $4 \leq HI$, high noncancer risk.

In this study, the health risk quotient for individual elements is denoted by $HQ_{ingestionx}$, $HQ_{dermalx}$, and HI_x, where "x" represents the specific trace element. For the aggregate of all trace elements, the health risk quotient is represented by $HQ_{ingestionTotal}$ (HQIT), $HQ_{dermalTotal}$ (HQDT), and HI_{Total}.

2.5. Multivariate statistical methods

Principal Component Analysis (PCA) is an essential statistical technique for transforming multivariate datasets, investigating interrelationships among data points and elucidating variable interactions (Bosnjak et al., 2012; Zhang et al., 2012; Devic et al., 2014). PCA reduces the dimensionality of datasets containing numerous correlated variables while preserving maximum variance. It enables systematic investigation of the impacts of water chemistry processes or human activities on groundwater composition (Hayton et al., 2004).

By implementing varimax orthogonal rotation to the principal components, PCA helps to identify interpretable factors related to hydrochemical or human-induced processes. This technique has been widely used in research on geothermal fluid migration processes, providing insights into source-specific geochemical signatures and anthropogenic impacts (Zhang et al., 2012; He et al., 2024).

3. Results

3.1. SOM clusters in water samples chemistry

A total of ten parameters (T, Na^+, pH, K^+, Ca^{2+}, Mg^{2+}, Cl^-, HCO_3^-, SO_4^{2-}, As) were used for the SOM-KM. The QE and TE were calculated for various map sizes. To choose the suitable map size, both the minimization of QE and TE and the reduction of empty output neurons were taken into account. After testing different configurations, a 100-neuron hexagonal grid was found to be the most suitable, yielding a QE of 1.114 and TE of 0.028. It effectively minimized the number of empty neurons. Consequently, the SOM algorithm generates a 100-hexagonal self-organized topological map. The SOM results were then used as input for KM clustering analysis to identify latent geochemical patterns (Zhuang et al., 2024). The optimal number of clusters, determined by both KM clustering and the DBI, was found to be six (Fig. 2b). The neurons' component planes were color-coded, with blue representing low values and red indicating high values. The inter-neuron chromatic coherence demonstrates parameter covariation between water sample parameters (Shen et al., 2023). By examining the color gradients across the component planes, the relationships between variables are revealed in an intuitive and clear manner (Mao et al., 2021).

Several significant findings are illustrated in Fig. 2a. From a distributional perspective, Na^+, Cl^-, and As may share a common source due to their similar spatial covariation patterns (Zhu et al., 2020; Tran et al., 2022). Neurons representing K^+ and HCO_3^- display strong covariation patterns, indicating a robust correlation between these ions. Moreover, the color variations observed in the concentrations of Ca^{2+} and SO_4^{2-} are analogous, suggesting that sulfate mineral dissolution may contribute to their presence. It is evident that there is no correlation among T, pH, and Mg^{2+}, as they do not exhibit similarities.

Fig. 2b depicts six clusters, revealing six distinct hydrochemical facies within the sampled water. These clusters are further supported by the Piper plots of six groups (Fig. 3a), which demonstrate the chemical composition and variation among the clusters.

3.2. Hydrochemical properties of water samples

Table S1 provides descriptive statistics of hydrochemical parameters of water samples. The sample T ranged from 3.3 °C to 82.5 °C, yielding a mean 23.9 °C. The total dissolved solids (TDS) varied between 21.54 mg/L and 9463.20 mg/L, with an average of 675.30 mg/L. The pH values ranged from 5.05 to 11.6, with a mean of 7.82, characterizing predominantly neutral to weakly alkaline. The average concentrations of major cations ranked as $Na^+ > Ca^{2+} > Mg^{2+} > K^+ > Li^+$, while for anions, the order was $HCO_3^- > SO_4^{2-} > Cl^- > NO_3^- > F^-$. Based on the SOM-KM analysis, the water samples were classified into six clusters. Table 1 provides the key hydrochemical parameters for each cluster, including the mean, minimum, and maximum values of T, pH, conductivity and major ions.

Piper diagram illustrates the hydrochemical types of hot springs in different clusters. Cluster 1 samples predominantly display the Na-HCO_3

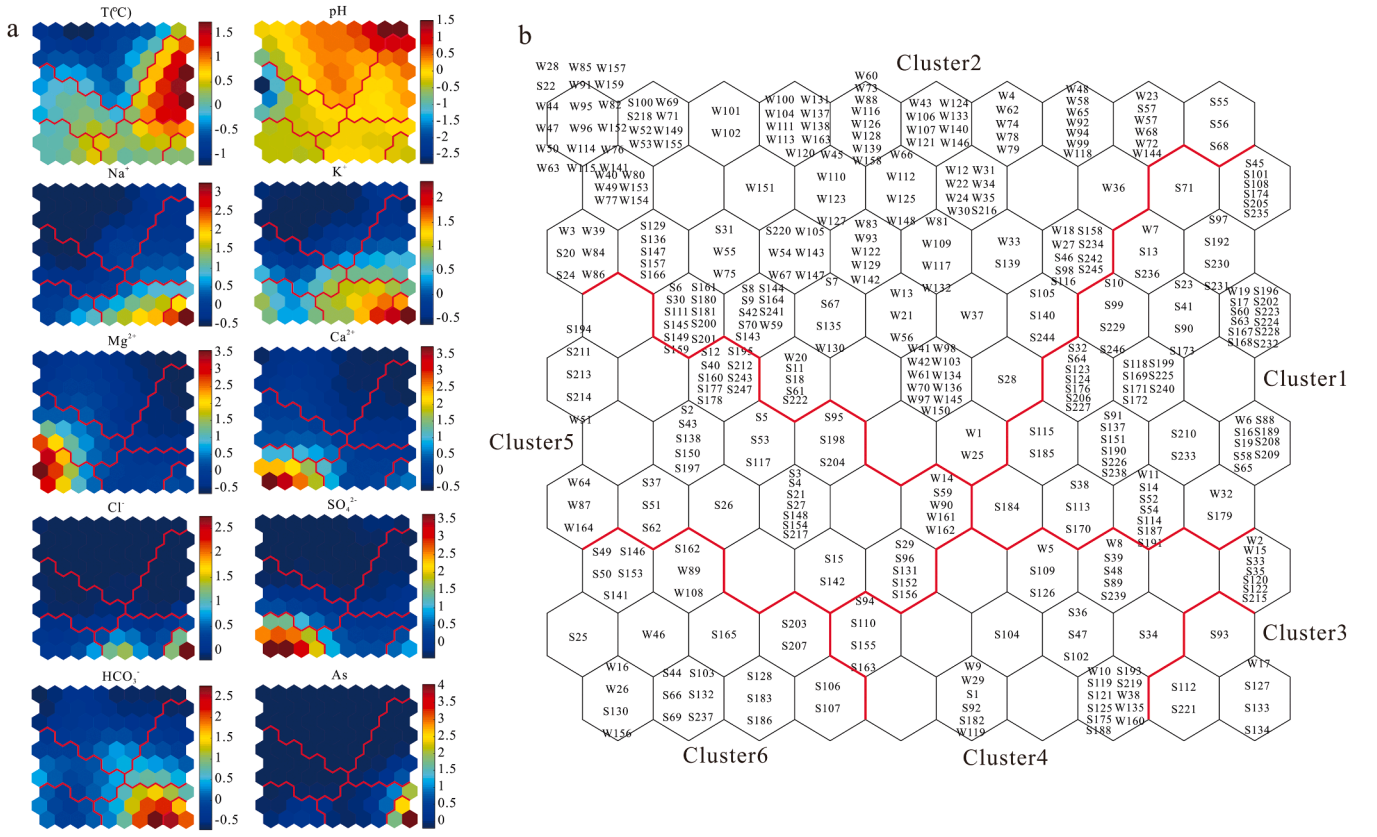

Fig. 2. (a) A spatial-organizing map (SOM) visualization of the topology of groundwater chemical parameters, with numbers indicating the values of the corresponding variables. (b) A SOM-KM clustering pattern, with numbers in the hexagons indicating groundwater samples.

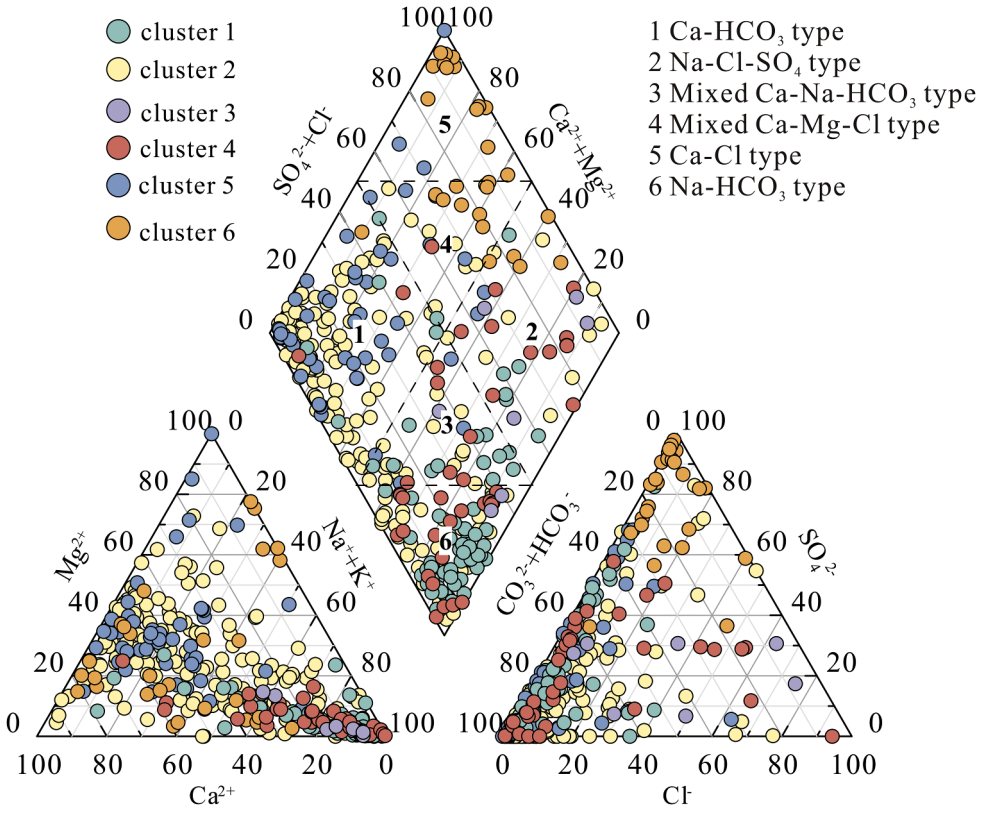

Fig. 3. Piper diagram of water samples from hot springs in the study area.

Table 1
The main parameters of main ion concentration and $\delta^{18}O$ and δD of each Cluster water sample.

		T (°C)	pH	conductivity us/cm	Li^+ mg/l	Na^+ mg/l	K^+ mg/l	Mg^{2+} mg/l	Ca^{2+} mg/l	F^- mg/l	Cl^- mg/l	Br^- mg/l	SO_4^{2-} mg/l	NO_3^- mg/l	$Y(CO_3^{2-})$ mg/l	$Y(HCO_3^-)$ mg/l	$\delta^{18}OV$-SMOW (‰)	δDV-SMOW (‰)
Cluster1	Average	69.0	7.99	775.89	0.61	157.49	11.33	5.09	24.46	8.99	21.72	0.12	79.00	2.58	44.89	344.25	-11.5	-84.2
	Min	38.0	6.83	3.00	0.04	9.54	0.36	0.06	0.55	0.30	1.61	0.10	4.17	0.11	9.90	27.57	-15.8	-120.6
	Max	95.0	9.25	1942.00	2.15	553.49	41.96	32.89	115.00	66.91	600.93	0.14	525.00	5.59	217.00	1009.67	-8.6	-59.6
Cluster2	Average	24.9	8.05	517.36	0.17	53.28	4.12	12.78	33.79	4.20	13.50	0.38	30.89	5.83	62.98	221.35	-11.3	-82.4
	Min	3.3	6.40	3.62	0.01	0.45	0.41	0.18	1.73	0.10	0.32	0.07	0.26	0.05	13.86	5.05	-16.3	-119.3
	Max	52.0	11.56	2569.00	2.00	484.86	50.93	44.28	111.58	24.31	122.37	0.58	639.03	92.95	222.21	882.62	-8.3	-54.0
Cluster3	Average	38.0	7.30	5462.57	1.86	1104.61	49.39	32.60	156.42	15.93	1067.57	3.31	620.99	17.49	322.67	1120.53	-13.1	-103.1
	Min	19.2	6.68	3347.00	0.91	517.91	15.31	1.27	53.35	1.24	116.42	1.07	104.87	3.17	295.67	213.01	-14.8	-118.5
	Max	50.3	8.15	13,720.00	2.63	2808.82	77.54	83.53	265.10	51.80	4502.46	7.50	1407.22	55.65	349.66	1990.62	-10.5	-88.6
Cluster4	Average	48.4	7.47	2021.12	0.77	433.07	24.24	16.64	79.54	5.41	159.63	2.41	268.68	6.45	145.56	902.95	-12.6	-95.4
	Min	15.4	5.05	3.00	0.11	7.42	2.26	0.69	1.31	0.44	0.53	0.04	0.35	0.04	6.46	84.52	-14.9	-118.6
	Max	72.3	9.82	3897.00	2.08	964.44	81.94	95.69	350.97	13.95	1013.36	5.15	695.64	51.27	358.59	2501.51	-9.2	-66.8
Cluster5	Average	39.8	7.33	937.13	0.42	57.58	12.12	39.29	94.14	3.81	25.20	3.81	101.52	6.31	66.01	418.13	-11.4	-84.1
	Min	5.0	6.63	3.45	0.02	1.97	1.11	9.25	15.09	0.20	0.29	0.07	0.03	0.10	12.54	113.15	-15.4	-117.0
	Max	61.8	8.20	2709.00	4.00	202.78	38.37	103.89	229.00	48.91	300.00	14.49	595.10	48.98	115.52	1151.73	-8.3	-59.2
Cluster6	Average	41.9	7.26	2490.75	0.38	225.10	17.34	88.99	345.92	3.60	128.45	0.09	1315.45	2.41	42.12	318.64	-12.7	-93.2
	Min	18.0	6.49	9.62	0.02	13.15	1.72	10.00	4.64	0.79	1.92	0.04	546.55	0.31	14.09	12.17	-16.4	-114.8
	Max	75.0	8.23	5039.00	2.16	760.39	42.27	220.91	691.29	8.16	828.25	0.16	2246.24	7.33	75.37	1516.53	-9.4	-65.3

type, while Cluster 2 is primarily characterized by Ca-HCO_3 and Na-HCO_3 types. Cluster 3 shows a predominant Na-Cl type, Cluster 4 is predominantly Na-HCO_3 type, Cluster 5 and Cluster 6 are predominantly Ca-HCO_3 and Ca-Cl type (Fig. 3). Geothermal fluids are susceptible to hydrochemical interaction and mixing, which can alter their physico-chemical signatures (Tong et al., 2000; Luo et al., 2023). Variations in ion concentration between distinct hot springs indicate discrete deep-circulation pathways. The differing hydrochemical types and compositions of spring water reflect varied circulation patterns within the study area. This finding corroborates earlier findings, indicating a more complex composition of hot springs (Bo et al., 2015; Zhang et al., 2016; Chen and Wang, 2021; Li et al., 2021, 2022; Wang et al., 2022; Zhou et al., 2022; Luo et al., 2023; Ouyang et al., 2023; He et al., 2024).

The water quality assessment was conducted in accordance with the WHO and Chinese National Guidelines (GB), which outline health reference limits for 15 trace elements, including B, Ba, Cd, Al, As, Cr, Cu, Mn, Mo, Fe, Hg, Pb, Sb, Tl, and Zn. The key statistical parameters (mean, minimum, and maximum values) of these trace elements from each cluster are summarized in Table 2.

3.3. Isotopic compositions of water samples

$\delta^{18}O$ and δD are critical tracers in hydrogeochemical studies, providing insights into geothermal water and understanding water-rock interactions (Tan et al., 2014; Pinti et al., 2021). To explore the origin and evolution of geothermal waters in Yunnan Province, $\delta^{18}O$ and δD values were analyzed. For well water, $\delta^{18}O$ values ranged from -16.3‰ to -8.3‰, while δD values ranged from -119.3‰ to -54.0‰. For hot spring water, $\delta^{18}O$ values ranged from -16.4‰ to -8.3‰, and δD values ranged from -120.6‰ to -59.2‰.

The $\delta^{18}O$ and δD values at the sampling points align closely with the global meteoric water line (GMWL) (Craig, 1961) (Fig. 4), indicating that atmospheric precipitation serves as the primary recharge source for the geothermal waters. As shown in Fig. 5a and b, certain hot springs in Clusters 1, 3, and 4 exhibit minor $\delta^{18}O$ enrichment, likely resulting from deeper water circulation and enhanced interactions with surrounding rocks, which facilitate isotopic exchange. The region influenced by the southwest monsoon receives the majority of its water vapor from the Indian Ocean (Kong et al., 2019). The average $\delta^{18}O$ and δD values show distinct patterns across the clusters: Cluster 1 averages -11.5‰ and -84.2‰, respectively; Cluster 2 averages -11.3‰ and -82.4‰; Cluster 3 averages -13.1‰ and -103.1‰; Cluster 4 averages -12.6‰ and -95.4‰; Cluster 5 averages -11.4‰ and -84.1‰; and Cluster 6 averages -12.7‰ and -93.2‰. Sampling sites in Cluster 1 are predominantly located in the southwest, followed by Clusters 2, 5, 6, and 4, while Cluster 3 sites are primarily situated in the northern part of the study area. The observed trend in the mean $\delta^{18}O$ and δD values becomes progressively depleted from the southwest (Cluster 1) to the north (Cluster 3). This pattern is primarily influenced by variations in altitude (Qu et al., 2018) as altitude-dependent fractionation induces isotopic depletion isotopic values due to equilibrium fractionation controlled by orographic cooling.

4. Discussion

4.1. Hydrochemical evolution and controlling factors

4.1.1. Water-Rock interaction signatures

The correlation between anion and cation concentrations in water provides valuable insights into the evolution of water chemistry (Zhou et al., 2023a). Elevated concentrations of HCO_3^- and Na^+ in most water samples suggest that carbonate and silicate minerals play a significant role in water-rock interactions. These minerals are closely involved in ion exchange and dissolution reactions, which in turn influence the chemical composition of the water. Fig. 5a shows that most water samples fall within the 4th quadrant, indicating that cation exchange is

Table 2
The main parameters of the concentration of trace elements in each cluster water sample.

		Hg	As	B	Mn	Cr	Cu	Zn	Mo	Cd	Sb	Ba	Tl	Pb	Fe	Al
		μg/L	μg/L	μg/L	μg/L	μg/L	μg/L	μg/L	μg/L	μg/L	μg/L	μg/L	μg/L	μg/L	μg/L	μg/L
Cluster1	Average	2.93	31.98	1302.69	46.87	2.76	3.02	16.63	1.51	0.02	5.30	199.03	0.34	1.58	478.87	137.07
	Min	0.10	0.48	4.17	0.17	0.08	0.04	0.51	0.01	0.01	0.01	0.14	0.01	0.01	0.01	0.76
	Max	39.10	152.00	7605.00	488.00	36.90	25.80	218.00	15.00	0.14	71.60	3016.00	4.00	22.70	15,162.00	3188.00
Cluster2	Average	0.39	8.06	253.28	18.23	1.56	1.88	7.44	4.83	0.40	0.53	221.74	0.21	1.40	185.07	52.52
	Min	0.11	0.61	0.44	0.07	0.03	0.03	0.41	0.03	0.01	0.01	0.36	0.01	0.01	0.12	0.12
	Max	0.91	67.07	3070.00	599.00	19.10	110.00	93.99	46.77	9.00	9.00	13,556.00	5.00	42.30	4525.00	2725.00
Cluster3	Average	0.65	858.81	9305.92	375.37	10.48	6.29	29.08	6.51	0.07	25.76	76.95	1.67	3.11	2575.93	834.77
	Min	0.21	313.00	3076.00	13.30	0.09	0.30	5.55	0.09	0.01	0.63	28.00	0.04	0.25	13.41	11.30
	Max	1.09	1912.00	21,007.00	1363.00	24.70	15.50	92.80	24.30	0.20	79.61	187.00	3.43	19.30	13,440.00	5641.00
Cluster4	Average	0.94	244.61	3160.66	81.14	8.83	11.61	16.46	4.66	1.17	14.76	364.24	0.71	1.10	1006.99	27.16
	Min	0.10	0.67	30.40	0.70	0.06	0.03	0.30	0.01	0.01	0.02	0.01	0.01	0.04	0.03	0.12
	Max	5.80	1345.00	22,089.00	371.00	199.00	306.35	135.00	43.14	26.60	105.00	6793.23	6.00	6.92	10,673.00	136.00
Cluster5	Average	0.61	11.43	277.07	71.94	3.59	2.09	14.03	2.47	0.23	3.29	107.61	0.54	1.52	293.63	15.58
	Min	0.26	0.62	2.12	0.09	0.07	0.24	1.08	0.10	0.01	0.01	4.45	0.01	0.01	0.04	0.26
	Max	0.95	57.80	1378.00	1181.58	39.60	18.90	135.00	29.02	6.00	41.50	450.00	4.00	11.30	2076.00	40.80
Cluster6	Average	0.15	67.77	936.19	94.26	3.85	6.43	30.27	14.26	0.22	2.50	29.53	0.34	1.40	2024.29	70.34
	Min	0.11	1.42	2.27	1.32	0.06	0.29	1.81	0.02	0.01	0.02	10.60	0.02	0.01	0.02	0.12
	Max	0.20	797.00	3751.00	402.00	33.10	25.80	341.00	150.29	3.21	14.90	55.98	0.94	7.97	28,577.00	1365.00

widespread in the study area. This exchange mainly involves Na^+-rich minerals (e.g., sodic feldspar and pyroxene) exchanging with dissolved Ca^{2+} and the elevated Na^+ concentrations are a common consequence of this process. In contrast, water samples from Cluster 2, 5 and 6 are located closer to the first quadrant, suggesting a relatively low degree of cation exchange in these waters. Specifically, Cluster 2 and 5 show Ca-HCO_3 water chemistry types, while Cluster 6 exhibits a Ca-Cl type, further confirming the limited cation exchange in these water types. Fig. 5b reveals that most water samples lie to the left of the 1:1 line, suggesting that Na^+ is not solely derived from the dissolution of rock salts, but also from the dissolution of silicate minerals or through ion exchange processes (He et al., 2024; Yan et al., 2024). During cation exchange, Na^+ is released into the water, which decreases the concentrations of Ca^{2+} and Mg^{2+}, while simultaneously promoting the dissolution of minerals like gypsum and increasing SO_4^{2-} concentrations. Fig. 5c illustrates that most water samples are located near or below the 1:1 line. This pattern indicates that the excess SO_4^{2-} may not only originate from gypsum dissolution, but also from the oxidation of $H_2S_{(g)}$ produced by deep fractures, especially under high temperature and pressure conditions. In such environments, H_2S oxidation significantly raises the SO_4^{2-} concentration (Xie et al., 2024). Furthermore, Fig. 5d shows that most water samples are positioned on either side of the $(Ca^{2+}+Mg^{2+})/HCO_3^-$ 1:1 line, indicating that their chemical compositions are not solely influenced by carbonate rock dissolution, but may also be affected by the dissolution of other minerals. Water samples from Clusters 2 and 3 are concentrated near the 1:1 line, suggesting that their circulation is predominantly shallow and controlled by mineral dissolution, with carbonate dissolution being the primary source of Ca^{2+} and Mg^{2+} (He et al., 2024). In contrast, elevated HCO_3^- levels in water samples from Clusters 1, 3, and 4 suggest that the dissolution of silicate minerals or interaction with CO_2-rich fluids may have contributed to water-rock interactions, resulting in higher concentrations of HCO_3^- (Vengosh et al., 2002; Tian et al., 2018). Finally, the elevated concentrations of Ca^{2+} and Mg^{2+} in water samples from Clusters 5 and 6 are likely due to gypsum dissolution, as supported by Fig. 5c. The subsequent reactions between the SO_4^{2-} from gypsum dissolution and calcium ions in the water lead to the increased concentrations of both Ca^{2+} and SO_4^{2-}. The observed variations in water-rock interaction processes can be attributed to differences in geological settings, mineral dissolution and fluid circulation conditions. The chemical characteristics of the water samples from different clusters suggest that mineral dissolution and cation exchange during their formation may vary, reflecting the complex water-rock interaction patterns in the study area. The following reactions summarize the primary processes influencing ion concentrations:

$$CaCO_{3(s)}+H_2O_{(l)}+CO_{2(g)} \rightarrow Ca^{2+}_{(aq)}+2HCO^-_{3(aq)}$$

$$CaSO_4 \bullet H_2O_{(s)} \rightarrow Ca^{2+}_{(aq)}+SO^{2-}_{4(aq)}+2H_2O_{(l)}$$

$$NaCl_{(s)} \rightarrow Na^+_{(aq)}+Cl^-_{(aq)}$$

$$NaAlSi_3O_{8(s)}+H_2O_{(l)} \rightarrow Na^+_{(aq)}+Al(OH)_{3(s)}+H_4SiO_{4(aq)}$$

$$CaMg(CO_3)_{2(s)}+H_2O_{(l)}+CO_{2(g)} \rightarrow Ca^{2+}_{(aq)}+Mg^{2+}_{(aq)}+HCO^-_{3(aq)}$$

4.1.2. *Multivariate statistical validation*

Building upon the hydrochemical signatures established by major ion correlations (Fig. 5), trace element analysis further delineates the complexity of water-rock interactions across clusters. Upon processing the trace element data, it was observed that hot spring water exhibited elevated levels of elements such as Li, As, B, Sr, Mn, and Fe. To bridge the gap between major ion dynamics (e.g., cation exchange and gypsum dissolution highlighted in Fig. 5) and trace element enrichment, PCA was performed by integrating both primary ions and trace elements. To enhance interpretation, variance explained by each component was

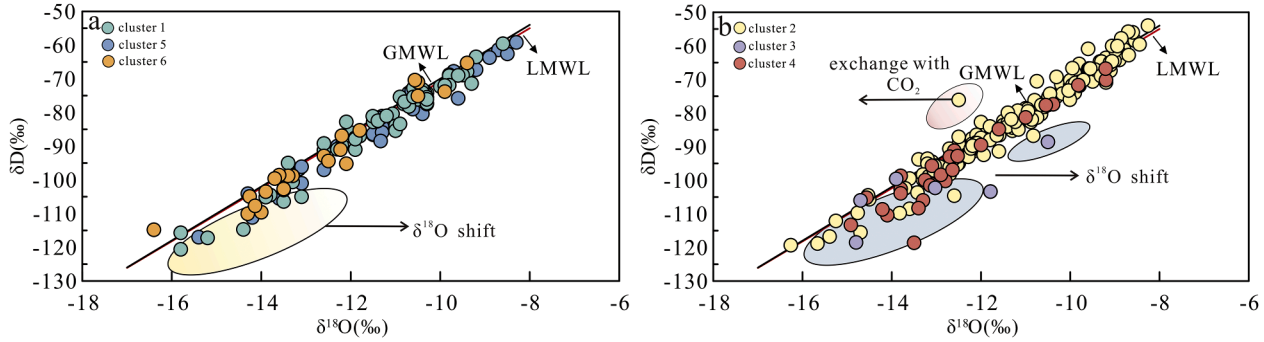

Fig. 4. Schematic of hydrogen and oxygen isotopes at sampling sites in the study area. (a) Cluster 1, 5, and 6 in water samples; (b) Cluster 2, 3, and 4 in water samples.

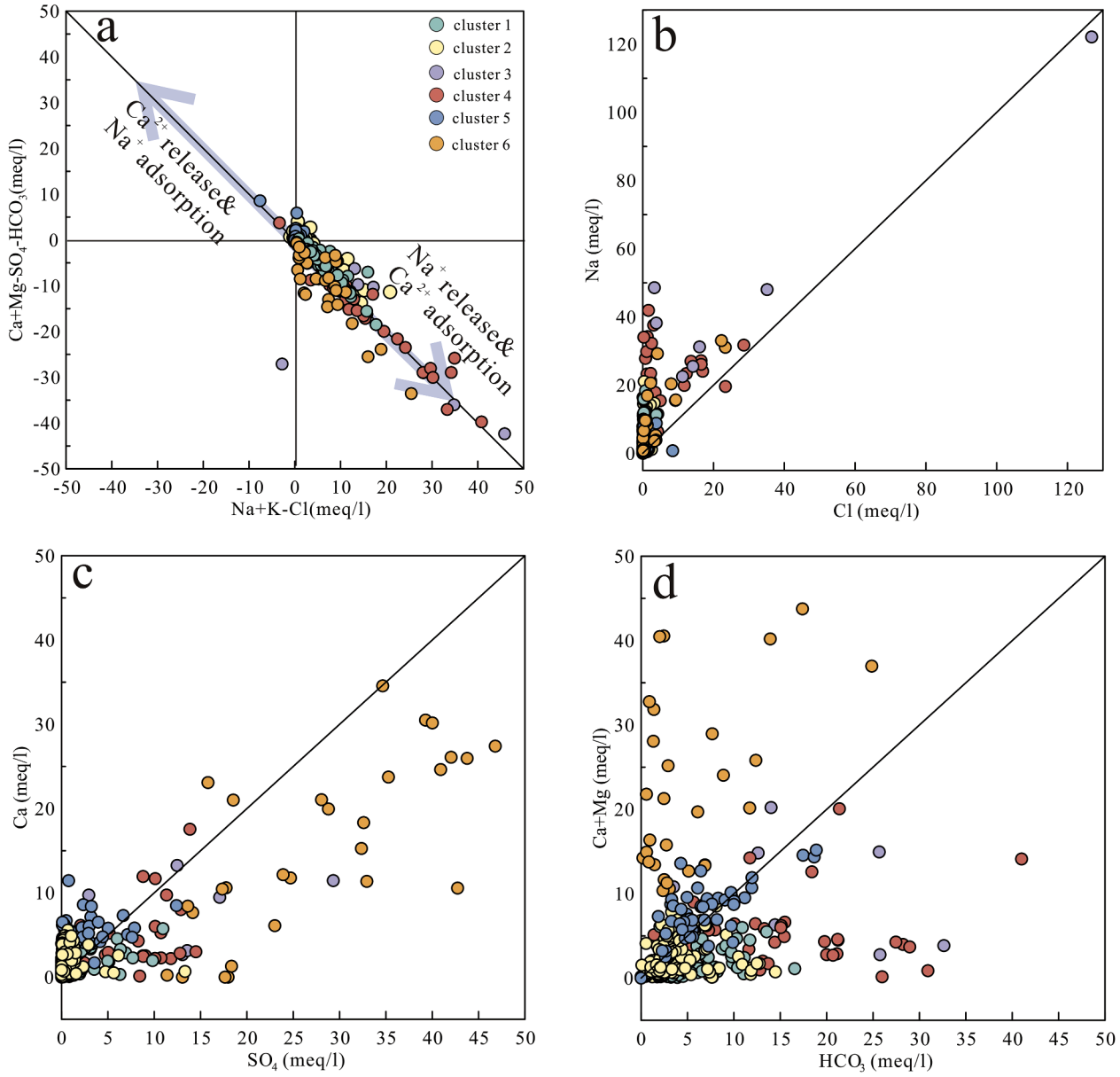

Fig. 5. The ion ratio map of the study area is presented below. (a) $(Na^+ + K^+ - Cl^-)/(Ca^{2+} + Mg^{2+} - SO_4^{2-} - HCO_3^-)$; (b) Cl^-/Na^+; (c) SO_4^{2-}/Ca^{2+}; (d) $HCO_3^-/(Ca^{2+} + Mg^{2+})$.

calculated with significance testing (Table 3). The first three components explained 35.03%, 16.87%, and 11.93% of the variance (totaling 63.83%) (Fig. 6), effectively capturing variability linked to distinct geological processes. Bartlett's test ($p < 0.001$) confirmed PCA suitability, and significance testing ($p < 0.05$) validated the first three components. These results extend the earlier findings on cation exchange and mineral dissolution (Fig. 5), explicitly connecting geochemical signatures to deep-seated magmatic-hydrothermal systems and shallow anthropogenic influences.

In water samples, SO_4^{2-}, Na^+, Cl^-, HCO_3^-, Li^+, As, Ca^{2+}, Sr exhibit high loadings on PC1 (35.03% variance). Furthermore Clusters 3, 4, 5 and 6 exhibited higher scores on PC1 (Fig. 7). This aligns with the deep-circulation water-rock interactions described in Fig. 5, where Na^+ enrichment from silicate dissolution (e.g., sodic feldspar) and SO_4^{2-} from gypsum/fluid oxidation dominate. Li correlates with lithium-bearing minerals (e.g., lithium mica) dissolved by geothermal fluids, while arsenic likely originates from syenite, arsenopyrite, or deep magmatic sources (Chen et al., 2015; Guo et al., 2017; Guan, 2018; He et al., 2024). The weak inter-element correlations (Table S6) suggest multiple pathways for As mobilization, potentially controlled by redox-sensitive mineral assemblages in the hydrothermal system. This hypothesis is supported by the widespread occurrence of hydrothermal minerals such as sulfates (gypsum, anhydrite), phyllosilicates (kaolinite, illite), and silica phases (opal) in the region (Zhang et al., 2008), which collectively create complex geochemical microenvironments governing arsenic speciation and transport. PC1 thus encapsulates the interplay of deep fluid circulation (with an average depth of 2.92 km) (Li et al., 2021; Li et al.,2022; Wang et al., 2022; Zhou et al., 2022; Luo et al., 2023; Ouyang et al.,2023; Li et al., 2024; He et al., 2024), magmatic and tectonic influences (Ke et al., 2022), corroborating the cation exchange processes and sulfate origins discussed in Fig. 5.

PC2 (16.87% variance) highlights Li-B enrichment coupled with Ca-Mg depletion, dominantly controlling Cluster 1 (Fig. 7). This dual influence suggests that carbonate dissolution contributes to the major ion chemistry of Cluster 1, while deep circulation (with an average depth of 4.13 km) (Li et al., 2021, 2022; Wang et al., 2022; Zhou et al., 2022; Ouyang et al., 2023; Li et al., 2024; He et al., 2024; Zhou et al., 2024) along active faults preferentially mobilizes Li and B through tourmaline and lepidolite dissolution (Zhang et al., 2024). The concurrent Ca-Mg depletion likely arises from two mechanisms: 1. Related to dissolution or cation exchange in evaporite rocks (Mao et al., 2021); 2. Although carbonate dissolution occurs, the deeper flow paths in Cluster 1 reduce recharge from fresh carbonate weathering, limiting Ca^{2+} and Mg^{2+} replenishment compared to shallow Clusters 2.

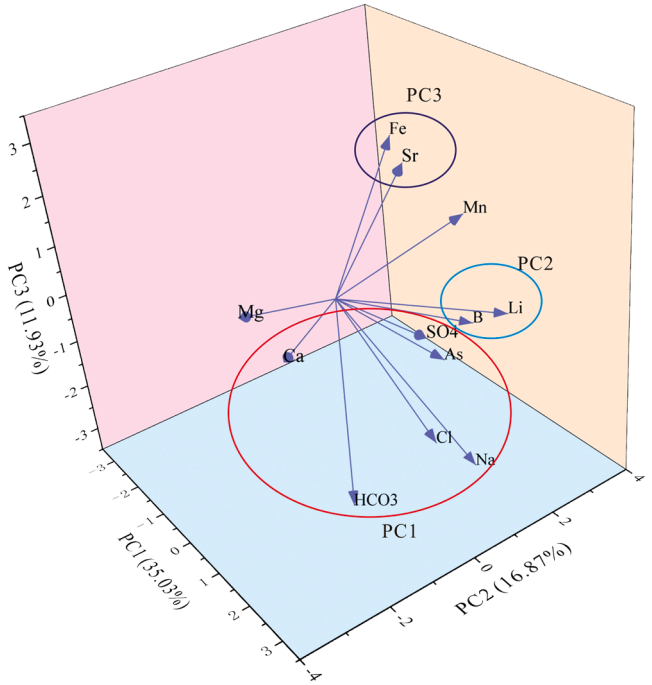

Fig. 6. 3-D rotated plot showing r-mode factor analysis of ionic correlations.

Table 3
Extraction sums of squared loadings.

Component	Total	% of variance	Cumulative %
1	4.204	35.032	35.032
2	2.024	16.867	51.899
3	1.431	11.928	63.826
4	0.892	7.429	71.256
5	0.752	6.27	77.525
6	0.672	5.601	83.127
7	0.604	5.037	88.163
8	0.505	4.208	92.372
9	0.369	3.079	95.45
10	0.28	2.336	97.787
11	0.169	1.405	99.192
12	0.097	0.808	100

Cluster 2 is predominantly influenced by PC3 (11.93% variance, Fig. 7), showing distinct Sr-Fe enrichment patterns. Fe primarily originates from igneous and sedimentary rocks (e.g., hematite), while Sr stems from strontianite and andesite. Weak Fe-Sr correlations (Table S6) and multifactorial controls suggest PC3 reflects combined shallow rock dissolution and anthropogenic inputs. Fe release arises from both pyrite oxidation in Fe-rich formations and iron infrastructure corrosion (Tao et al., 2023; Zhou et al., 2023b; Amin et al., 2024), while Sr enrichment is driven by strontium minerals weathering and minor agricultural amendments. Despite anthropogenic contributions, shallow carbonate dissolution remains the dominant Sr source. PC3 thus integrates natural water-rock interactions and human activities, illustrating complex hydrochemical dynamics. The possible chemical reaction is as follows:

$$Ca_3(AsO_4)_{2(s)}+6H^+_{(aq)} \rightarrow 3Ca^{2+}_{(aq)}+2H_3AsO_{4(s)}$$

$$FeAsS_{(s)}+11/4O_{2(g)}+5/2H_2O_{(l)} \rightarrow Fe^{3+}_{(aq)}+H_2AsO^-_{4(aq)}+SO^{2-}_{4(aq)}+2H^+_{(aq)}$$

$$LiAlSi_2O_{6(s)}+4H^+_{(aq)} \rightarrow Li^+_{(aq)}+Al^{3+}_{(aq)}+2H_4SiO_{4(aq)}$$

$$NaFe_3Al_6(BO_3\ \ )_3\ \ Si_6O_{18}(OH)_{4(s)}+16H^+_{(aq)} \rightarrow 3Fe^{2+}_{(aq)}+6Al^{3+}_{(aq)}+3B(OH)_{3(l)}\ \ +6H_4SiO_{4(aq)}+Na^+_{(aq)}+2H_2\ \ O_{(l)}$$

$$Fe_3O_{4(s)}+8H^+_{(aq)} \rightarrow 2Fe^{2+}_{(aq)}+Fe^{3+}_{(aq)}+4H_2\ \ O(l)$$

$$SrAl_2Si_2O_8(s)+8H^+_{(aq)} \rightarrow Sr^{2+}_{(aq)}+2Al^{3+}_{(aq)}+2H_4\ \ SiO_{4(aq)}$$

4.2. Comprehensive geothermal water quality assessment

Considering the WQI values, it was determined that excellent quality (84.71%), good (6.07%), fair (3.16%), poor (1.45%), and unsatisfactory (4.61%). The data indicate that most of the water samples were of good quality, making them suitable for human consumption and domestic use. However, 9.22% of the water samples exhibited substandard quality (WQI>100), predominantly distributed in PC1-controlled Clusters 3–6 (Fig. 8). According to Table S3, the WQI values for all trace elements, except for arsenic, remained within the safe range. It is noteworthy that water samples from Cluster 3 exhibited high arsenic concentrations, resulting in low WQI values that fell within the danger zone. This aligns with PC1's deep-circulation signature where arsenic enrichment via sulfide oxidation and silicate weathering (Fig. 5) deteriorates water quality. Cluster 1 (PC2- controlled) showed localized risks in samples, likely due to deep Li-B mobilization along fault zones. In contrast, PC3-driven Cluster 2 maintained compliance with WHO standards, consistent with its shallow aquifer characteristics. This observation aligns with

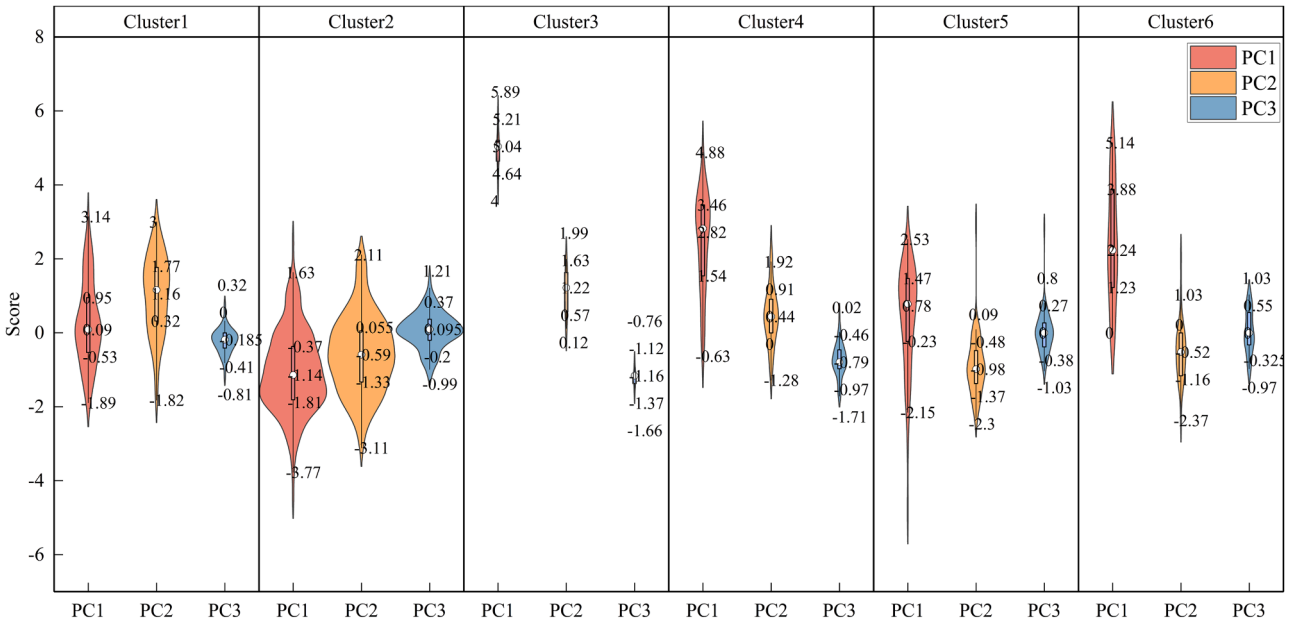

Fig. 7. Violin plots of 3 PC scores on various water samples.

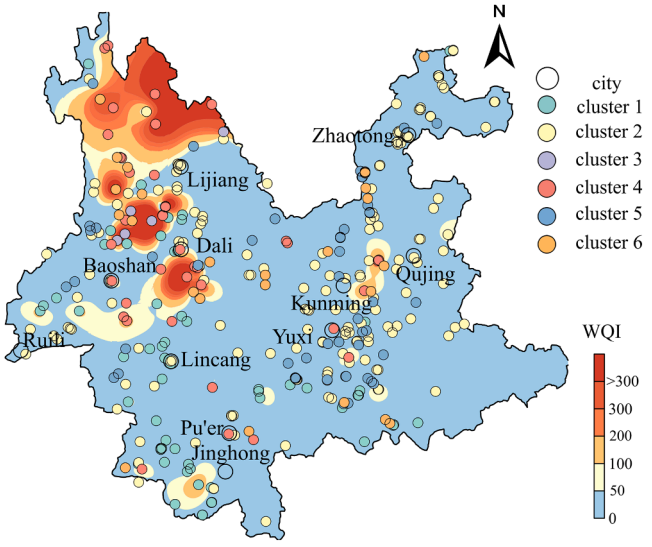

Fig. 8. Spatial distribution of water quality assessment in the study area.

findings from previous studies on the link between elevated arsenic concentrations and geothermal activity. The previous studies include research from the United States (Langner et al., 2001; McCleskey et al., 2022), New Zealand (McLaren and Kim, 1995), Japan (Ogawa et al., 2012; Hama et al., 2023), France (Barats et al., 2014), and China's Yangbajing geothermal field (Li et al., 2003; Guo et al., 2008; Wang and Cheng, 2023). These studies confirm a close relationship between geothermal processes and high arsenic concentrations, with geothermal activity widely recognized as a key mechanism for arsenic migration from rocks to water (Hama et al., 2023; Wang and Cheng, 2023; Yan et al., 2024; Zhuang et al., 2024). Specifically, higher temperatures increase arsenic solubility, enhancing arsenopyrite oxidative dissolution. High salinity alters the water's chemical properties, promoting further arsenic dissolution, while weakly alkaline conditions favour arsenic in its soluble form, enhancing its mobility. The long-term interaction between geothermal water and rock minerals, including mineral dissolution and water-rock reactions, provides a continuous source of arsenic. Additionally, geothermal activity in the aquifer creates favourable physicochemical conditions, such as specific redox conditions and pH levels, which facilitate the release and migration of arsenic. As a result, elevated arsenic concentrations due to geothermal processes are a major factor in water quality deterioration, posing significant challenges to the sustainable use of geothermal water resources and ensuring water quality safety.

Given these findings, it is recommended that relevant authorities strengthen monitoring of arsenic concentrations in groundwater, especially in regions with high geothermal activity. Regular monitoring and assessment programs should be implemented to ensure the safety of water sources and mitigate potential health risks. By taking timely measures to improve water quality, the harmful effects of arsenic on human health can be minimized.

4.3. *Detailed human health risk evaluation*

Fig. 9 shows that total HI_{Total} for both adults and children exceed 1 in PC1-dominated Clusters 3–6, indicating elevated non-carcinogenic risks from trace elements. The spatial HI_{Total} gradient (northwest > periphery) mirrors PC1′s geochemical footprint of deep fluid upwelling. This pattern can be attributed to variations in geological frameworks, hydrodynamic regimes, and anthropogenic inputs, which affect the mobilization-transport-sequestration cycles of trace elements in water bodies.

Further analysis reveals that the health risks from ingestion were higher than dermal exposure (Jiang et al., 2021), particularly severe in Cluster 3–6 (PC1-controlled). Cluster 1 (PC2-controlled) exhibited moderate risks of samples, PC3- driven Cluster 2 maintained HI_{Total} <1 across most samples. In Fig. 9 and Table S4, the HQIT, HQDT and HI_{total} values for children are notably higher than those for adults, indicating that children are more susceptible to the adverse effects of trace elements when exposed to the same water media (Tong et al., 2021). This heightened vulnerability is linked to the physiological characteristics of children, whose liver, kidneys and immune systems are still developing, making them less efficient in eliminating harmful substances from the body. Additionally, children have a larger body surface area relative to their body weight, meaning that the concentration of the same amount of pollutants in their bodies may be higher, thereby increasing their health risks.

Table S4 shows that the total HI_{total} for trace elements exceeds 1,

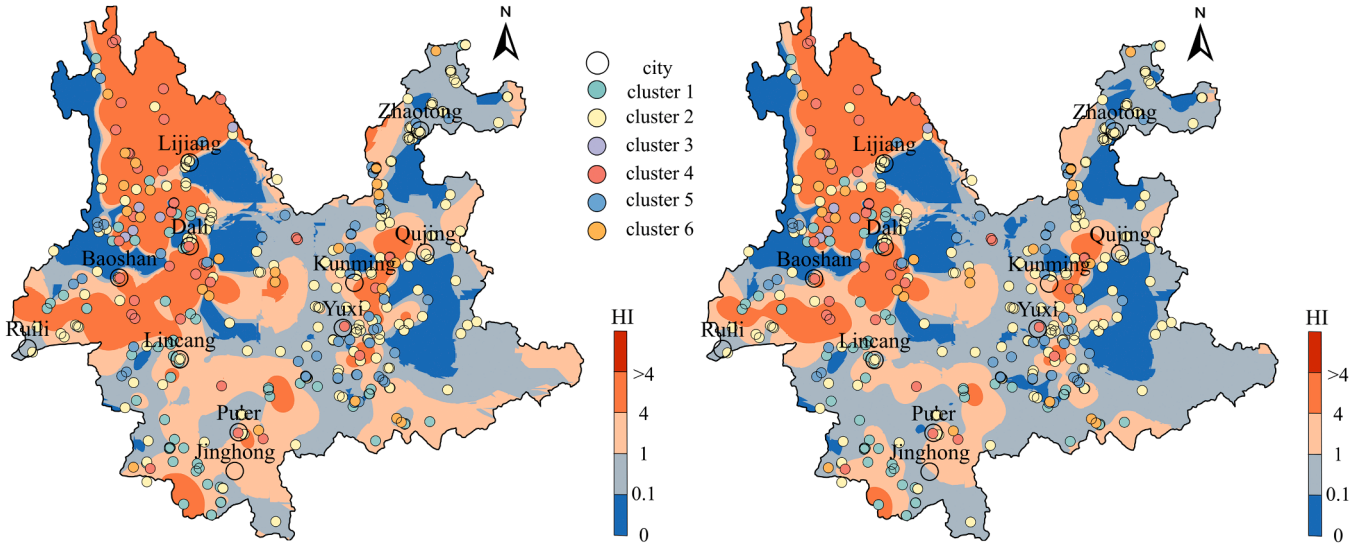

Fig. 9. Map of human health risk distribution in the study area. (a) HI_{Total} map for children; (b) HI_{Total} map for adults.

primarily due to the HI values of HI_{As} and HI_{Sb} (Tables S8 and S9) in geothermal water exceeding 1 for both adults and children. This indicates that the presence of As and Sb in geothermal water may pose non-carcinogenic risks to human health. As is a known carcinogen and prolonged exposure to high concentrations of As in water can lead to various health issues, including skin lesions, lung cancer, bladder cancer and liver cancer (Hama et al., 2023; Zhuang et al., 2024). In high-temperature, alkaline environments, the concentration of As in geothermal water is particularly high, primarily due to the dissolution of minerals and interactions between the water and rocks. The toxic effects of As intensify with increased exposure duration, making the As concentration in geothermal water a critical factor for health risk assessment. While Sb is not as widely recognized as arsenic, long-term exposure to high concentrations of antimony can also have detrimental effects. Antimony can bind with thiol groups in the body, inhibiting the activity of enzymes such as thiolase, disrupting intracellular ion balance, causing potassium deficiency and leading to metabolic disorders that affect multiple systems and organs (Li et al., 2019c; Wen et al., 2023). Sb shares similar chemical properties with As and possesses certain toxicity, likely related to the dissolution of minerals and the weathering of rocks in geothermal systems.

Spatial analysis demonstrates that high-risk zones (Fig. 9) align with PC1-driven clusters (3–6), where deep-circulation fluids enrich As and Sb via sulfide oxidation and silicate weathering. In contrast, the low-risk waters of Cluster 2, controlled by PC3 processes, remain confined to shallow aquifers with limited water-rock interaction. These findings validate that arsenic anomalies in Clusters 3–6 originate from deep magmatic-hydrothermal systems, while Clusters 1 and 5–6 reflect mixing of karst-derived solutes (high Ca^{2+} and SO_4^{2-}; Fig. 5c) with tectonically mobilized elements. The PCA thus bridges molecular-scale mineral reactions (e.g., arsenopyrite oxidative dissolution) to regional-scale health risks, establishing a mechanistic framework for water quality management in geothermal terrains.

5. Water quality improvement and management strategies

There are notable spatial variations in water quality across the study area. In the northwestern regions, including Lijiang, Lincang, Kunming, Baoshan, Jinghong, Pu'er, and Dali (Figs. 8 and 9), water quality is generally poor as it contains elevated concentrations of As and Sb. In contrast, regions like Qujiang, Zhaotong, Yuxi, and Ruili (Figs. 8 and 9) exhibit good water quality, meeting drinking water standards and posing minimal health risks. In these areas, maintaining water quality through regular monitoring and protecting aquifer zones is crucial. Increasing public awareness and improving water source protection are also essential for long-term sustainability.

The spatial distribution of water quality reflects the influence of geological conditions, geothermal water flow and water-rock interactions. Poorer water quality in the northwest is likely linked to arsenic- and antimony-rich minerals, while better quality in the central region is attributed to favorable recharge conditions and lower human impact.

In this study, water samples in Cluster 1, including s163, s167, s168, s189, s196, and s228, exhibit high temperatures exceeding 90 °C, making them suitable for geothermal energy development, particularly for geothermal power plants (Peng et al., 2023; Wang et al., 2024). However, some other points within Cluster 1, while not reaching 90 °C, still maintain enthalpy conditions suitable for direct-use geothermal systems, such as greenhouse heating and aquaculture. Additionally, water samples in Cluster 2 show significant potential for tourism development. The favorable water quality in this area supports the construction of hot spring resorts, wellness centers and facilities for drinking and irrigation. Hot spring tourism is a globally recognized sustainable industry, contributing substantially to economic growth and regional tourism diversification.

However, water samples from Clusters 3, 4, 5, and 6 correspond to regions with poor water quality, primarily due to high concentrations of arsenic and other harmful trace elements. It is crucial to increase monitoring efforts in these regions and implement effective treatment solutions, such as arsenic removal technologies (e.g., iron-based adsorbents and membrane filtration) and conducting regular monitoring (Bissen and Frimmel, 2003; Mohan and Pittman, 2007; Ramos et al., 2009; Siddique et al., 2020; Alazaiza et al., 2021; Samuel et al., 2022; Priya et al., 2022), to improve water quality and mitigate health risks. Especially in residential areas near water sources and public health education on arsenic exposure should be strengthened to protect the local population.

Overall, the region has significant potential for geothermal energy development, but it requires careful planning and responsible utilization. Geothermal power generation and hot spring tourism offer opportunities for sustainable energy production and economic growth. However, it is essential to ensure environmental protection and water quality safety throughout the development process to prevent further geothermal water pollution. Comprehensive assessment and rational planning of geothermal water resources are critical to achieving long-term sustainability in the region.

6. Conclusion

Combining SOM-KM clustering, PCA analysis and hydrochemical methods, this study systematically evaluated the water quality characteristics of geothermal water in Yunnan Province and its associated health risks, leading to the following conclusions:

(1) Geothermal water in the study area was found to be moderately to weakly alkaline. After SOM-KM classification, all water samples were divided into six clusters, each exhibiting distinct water chemistry types: Na-HCO_3 (Clusters 1 and 4), Ca-HCO_3 (Clusters 2 and 5), Na-Cl (Cluster 3), and Ca-Cl (Cluster 6). Stable isotope analyses revealed that water in the study area was primarily recharged by atmospheric precipitation, with different altitudes influencing the water source.
(2) PCA indicates that the spatial variability in geothermal water quality is mainly influenced by deep hydrological cycles and magma-tectonic interactions, with arsenic enrichment in high-risk areas. PC1 is closely related to water-rock interactions and high-temperature conditions, particularly in arsenic-enriched regions. PC2 is associated with regional tectonics (e.g., faults and groundwater flow) that affect water quality distribution, while PC3 reflects the combined influence of shallow rock dissolution and anthropogenic activities such as corrosion of iron-based infrastructure and agricultural practices.
(3) Water quality shows significant spatial variability within the study area. The northwestern region (e.g., Lijiang, Lincang, Kunming, Pu'er) exhibits poor water quality, high non-carcinogenic risks and hence, unsuitable for drinking. In contrast, the central region displays better water quality, meeting drinking water standards. This disparity may be due to arsenic release from mineral dissolution in the high-temperature and weakly alkaline environment in the northwest. At the same time, the central region benefits from better groundwater recharge conditions and less human activity.

By integrating multiple analytical methods, this study offers the first insights into the spatial distribution of geothermal water quality and health risks, revealing the potential sources and mechanisms of trace element distribution within the hydrogeological context. Future research should focus on continuous monitoring of trace elements, particularly arsenic, further detailed geochemical modelling of groundwater-rock interactions and evaluating the impact of anthropogenic activities on groundwater quality. Additionally, investigating contamination sources and developing strategies to mitigate health risks are essential. Overall, this comprehensive evaluation reveals both the development potential and health risks of Yunnan's geothermal resources, where the quantified arsenic enrichment mechanisms necessitate groundwater monitoring frameworks that balance utilization benefits with public health safeguards, providing valuable insights into hydrogeology.

Funding

The work was funded by Deep Earth Probe and Mineral Resources Exploration - National Science and Technology Major Project (2024ZD1000503), National Key Research and Development Project (2023YFC3012005-1), Central Public-interest Scientific Institution Basal Research Fund (CEAIEF20240405, CEAIEF2022030200, CEAIEF2022030205, CEAIEF20240207), the National Natural Science Foundation of China (41673106,41403099), and IGCP Project 724.

CRediT authorship contribution statement

Zhaojun Zeng: Writing – review & editing, Writing – original draft, Methodology, Conceptualization. **Li Yang:** Visualization, Software, Formal analysis, Conceptualization. **Yueju Cui:** Writing – original draft, Software, Funding acquisition, Formal analysis. **Xiaocheng Zhou:** Investigation, Funding acquisition, Conceptualization. **Miao He:** Resources, Investigation. **Yuwen Wang:** Resources, Investigation. **Yucong Yan:** Resources, Investigation. **Bingyu Yao:** Resources, Investigation. **Xiaojing Hu:** Validation, Data curation. **Weiye Shao:** Validation, Data curation. **Jian Li:** Validation, Data curation. **Hong Fu:** Validation, Data curation.

Declaration of competing interest

The authors declare that they have no known competing financial interests or personal relationships that could have appeared to influence the work reported in this paper.

Supplementary materials

Supplementary material associated with this article can be found, in the online version, at doi:10.1016/j.geothermics.2025.103323.

Data availability

Data will be made available on request.

References

Abbasnia, A., Radfard, M., Mahvi, A.H., Nabizadeh, R., Yousefi, M., Soleimani, H., Alimohammadi, M., 2018. Groundwater quality assessment for irrigation purposes based on irrigation water quality index and its zoning with GIS in the villages of Chabahar, Sistan and Baluchistan, Iran. Data Brief 19, 623–631.
Alazaiza, M.Y.D., Albahnasawi, A., Ali, G.A.M., Bashir, M.J.K., Copty, N.K., Amr, S.S.A., Abushammala, M.F.M., Al Maskari, T., 2021. Recent advances of nanoremediation technologies for soil and groundwater remediation: a review. Water 13 (16), 2186.
Amin, S., Kazama, S., Sawangjang, B., Takizawa, S., 2024. Causes and effects of scale deposition in water supply pipelines in Surakarta City, Indonesia. Water 16 (16), 2275.
Andrén, M., Stockmann, G., Skelton, A., Sturkell, E., Mörth, C.M., Guðrúnardóttir, H.R., Keller, N.S., Odling, N., Dahrén, B., Broman, C., Balic-Zunic, T., Hjartarson, H., Siegmund, H., Freund, F., Kockum, I., 2016. Coupling between mineral reactions, chemical changes in groundwater, and earthquakes in Iceland. J. Geophys. Res. Solid Earth 121 (4), 2315–2337.
Astel, A., Tsakouski, S., Barbieri, P., Simeonov, V., 2007. Comparison of self-organizing maps classification approach with cluster and principal components analysis for large environmental data sets. Water Res. 41 (19), 4566–4578.
Bai, S., 2008. Research On Inducing Mechanism and Countermeasures for Geological Hazards For Highway Projects in Geologically Complicated Areas in Yunnan [Doctoral]. Kuming University of Science and Technology.
Bao, Z., Hu, L., Xiao, J., Zha, X., Lv, J., Zhao, Y., 2023. Stable isotopes and hydrogeochemical evolutions of groundwater from a typical seismic fault zone in the Mt. Lushan region, Eastern China. Front. Earth Sci. 11.
Barats, A., Féraud, G., Potot, C., Philippini, V., Travi, Y., Durrieu, G., Dubar, M., Simler, R., 2014. Naturally dissolved arsenic concentrations in the Alpine/Mediterranean Var River watershed (France). Sci. Total. Environ. 473, 422–436.
Bissen, M., Frimmel, F.H., 2003. Arsenic — a review. Part II: oxidation of Arsenic and its removal in water treatment. Acta hydrochim. Hydrobiol. 31 (2), 97–107.
Bo, Y., Liu, C., Zhao, Y., Wang, L., 2015. Chemical and isotopic characteristics and origin of spring waters in the Lanping–Simao Basin, Yunnan, Southwestern China. Geochemistry 75 (3), 287–300.
Bosnjak, M., Capak, K., Jazbec, A., Casiot, C., Sipos, L., Poljak, V., Dadic, Z., 2012. Hydrochemical characterization of arsenic contaminated alluvial aquifers in Eastern Croatia using multivariate statistical techniques and arsenic risk assessment. Sci. Total Environ. 420, 100–110.
Cacciapuoti, S., Luciano, M., Megna, M., Annunziata, M., Napolitano, M., Patruno, C., Scala, E., Colicchio, R., Pagliuca, C., Salvatore, P., Fabbrocini, G., 2020. The role of thermal water in chronic skin diseases management: a review of the literature. J. Clin. Med. 9 (9), 3047.
Chen, L., Wang, G., 2021. Hydrochemical changes of a spring due to the May 30, 2014 Ms 6.1 Yingjiang earthquake, southwest China. Environ. Pollut. 284, 117125.
Chen, Y., Liu, J., 2023. Groundwater trace element changes were probably induced by the M_L3.3 earthquake in Chaoyang district, Beijing. Front. Earth Sci. 11, 1260559.
Chen, Y., Yang, L., Li, K., Xie, K., Ji, K., 2015. Geophysical Geochemical Atlas of Yunnan Province. Geology Press, Beijing.
Coyte, R., McKinley, K., Jiang, S., Karr, J., Dwyer, G., Keyworth, A., Davis, C., Kondash, A.J., Vengosh, A., 2020. Occurrence and distribution of hexavalent chromium in groundwater from North Carolina, USA. Sci. Total Environ. 711, 135135.
Craig, H., 1961. Isotopic variations in meteoric waters. Science 133, 1702–1703.

Devic, G., Djordjevic, D., Sakan, S., 2014. Natural and anthropogenic factors affecting the groundwater quality in Serbia. Sci. Total Environ. 468, 933–942.
Fagundo-Castillo, J., Carrillo-Rivera, J., Antigueredad-Auzmendi, I., González-Hernández, P., Peláez-Díaz, R., Hernández-Díaz, R., Cáceres-Govea, D., Hernández-Santana, J., Suárez-Muñoz, M., Melián-Rodríguez, C., Rodríguez-Piña, M., 2008. Chemical and geological control of spring water in Eastern Guaniguanico mountain range, Pinar del Rio, Cuba. Environ. Geol. 55 (2), 247–267.
Fan, Y., Li, M., Fu, T., Yubing, S., Dong, J., 2015. Study on distribution characteristics and cause analysis of the Eryuan Basin geothermal area. Resour. Environ. Eng. 29 (05), 701–705.
Githaiga, K., Njuguna, S., Gituru, R., Yan, X., 2021. Water quality assessment, multivariate analysis and human health risks of heavy metals in eight major lakes in Kenya. J. Environ. Manage. 297, 113410.
Guan, X., 2018. Study On Risk Assessment of Landslide in Yunnan Province [Doctoral]. China University of Mining and Technology (Beijing).
Guo, Q., Planer-Friedrich, B., Liu, M., Li, J., Zhou, C., Wang, Y., 2017. Arsenic and thioarsenic species in the hot springs of the Rehai magmatic geothermal system, Tengchong volcanic region, China. Chem. Geol. 453, 12–20.
Guo, Q., Planer-Friedrich, B., Yan, K., 2021. Tungstate thiolation promoting the formation of high-tungsten geothermal waters and its environmental implications. J. Hydrol. 603, 127016.
Guo, Q., Wang, Y., Liu, W., 2008. B, As, and F contamination of river water due to wastewater discharge of the Yangbajing geothermal power plant, Tibet, China. Environ. Geol. 56 (1), 197–205.
Hakimi, Y., Orban, P., Deschamps, P., Brouyere, S., 2021. Hydrochemical and isotopic characteristics of groundwater in the Continental Intercalaire aquifer system: insights from Mzab Ridge and surrounding regions, North of the Algerian Sahara. J. Hydrol.: Region. Stud. 34, 100791.
Hama, T., Ito, H., Kawagoshi, Y., Nakamura, K., Kubota, T., 2023. Natural attenuation and remobilization of arsenic in a small river contaminated by the volcanic eruption of Mount Iou in southern Kyushu Island, Japan. J. Hazard. Mater. 455, 131576.
Haselbeck, V., Kordilla, J., Krause, F., Sauter, M., 2019. Self-organizing maps for the identification of groundwater salinity sources based on hydrochemical data. J. Hydrol. 576, 610–619.
Hayton, J., Allen, D., Scarpello, V., 2004. Factor retention decisions in exploratory factor analysis: a tutorial on parallel analysis. Org. React. Mech. 7 (2), 191–205.
He, P., Zhang, H.R., Li, S., Zhou, X., Zhou, X., He, M., Tian, J., Zhang, Y., Wu, Z., Chen, T., Liu, Y., Aldahan, A., Huang, Y., 2024. Geological and hydrochemical controls on water chemistry and stable isotopes of hot springs in the Three Parallel Rivers Region, southeast Tibetan Plateau: the genesis of geothermal waters. Sci. Total Environ. 906, 167648.
Hosono, T., Hartmann, J., Louvat, P., Amann, T., Washington, K., West, A., Okamura, K., Böttcher, M.E., Gaillardet, J., 2018. Earthquake-induced structural deformations enhance long-term solute fluxes from active volcanic systems. Sci. Rep. 8, 14809.
Jiang, C., Zhao, Q., Zheng, L., Chen, X., Li, C., Ren, M., 2021. Distribution, source and health risk assessment based on the Monte Carlo method of heavy metals in shallow groundwater in an area affected by mining activities, China. Ecotox. Environ. Safe 224, 112679.
Ke, X., Li, Y., Wang, W., Niu, F., Gao, Z., 2022. Hydrogeochemical characteristics and processes of thermokarst lake and groundwater during the melting of the active layer in a permafrost region of the Qinghai-Tibet Plateau, China. Sci. Total Environ. 851, 158183.
Kim, K., Yun, S., Yu, S., Choi, B., Kim, M., Lee, K., 2020. Geochemical pattern recognitions of deep thermal groundwater in South Korea using self-organizing map: identified pathways of geochemical reaction and mixing. J. Hydrol. 589, 125202.
Kong, Y., Wang, K., Li, J., Pang, Z., 2019. Stable isotopes of precipitation in China: a consideration of moisture sources. Water 11 (6), 1239.
Krishan, G., Kumar, M., Rao, M., Garg, R., Yadav, B., Kansal, M., Singh, S., Bradley, A., Muste, M., Sharma, L., 2023. Integrated approach for the investigation of groundwater quality through hydrochemistry and water quality index (WQI). Urban Clim. 47, 101383.
Langner, H., Jackson, C., McDermott, T., Inskeep, W., 2001. Rapid oxidation of arsenite in a hot spring ecosystem, Yellowstone National Park. Environ. Sci. Technol. 35 (16), 3302–3309.
Lee, K., Yun, S., Yu, S., Kim, K., Lee, J., Lee, S., 2019. The combined use of self-organizing map technique and fuzzy c-means clustering to evaluate urban groundwater quality in Seoul metropolitan city South Korea. J. Hydrol. 569, 685–697.
Li, B., Shi, Z., Wang, G., Liu, C., 2019a. Earthquake-related hydrochemical changes in thermal springs in the Xianshuihe Fault zone, Western China. J. Hydrol. 579, 124175.
Li, C., Zhou, X., He, M., Zeng, Z., Wang, Y., Tian, J., Yan, Y., Yao, B., Su, H., Zhou, H., Li, R., 2024. Structural controls and Earthquake response of thermal fluids geothemistry, Southern Yunnan, Southeastern Tibetan Plateau. J. Hydrol. Under review.
Li, C., Zhou, X., Yan, Y., Ouyang, S.P., Liu, F., 2021. Hydrogeochemical characteristics of hot springs and their short-term seismic precursor anomalies along the Xiaojiang Fault Zone, Southeast Tibet Plateau. Water 13 (19), 2638.
Li, D., Chang, F., Wen, X., Duan, L., Zhang, H., 2022a. Seasonal variations in water quality and algal blooming in hypereutrophic Lake Qilu of southwestern China. Water 14 (17), 2611.
Li, H., He, X., Hu, X., Duo, J., 2003. Environmental issues of geothermal development in Yangbajing, Tibet and the countermeasures. Wuhan Univ. J. Nat. Sci., 8 (3B), 965–974.
Li, L., Tu, H., Zhang, S., Wu, L., Wu, M., Tang, Y., Wu, P., 2019b. Geochemical behaviors of antimony in mining-affected water environment (Southwest China). Environ. Geochem. Health 41 (6), 2397–2411.
Li, P., Tian, R., Liu, R., 2019c. Solute geochemistry and multivariate analysis of water quality in the Guohua phosphorite mine, Guizhou Province, China. Expos. Health 11 (2), 81–94.
Li, T., Sun, G., Yang, C., Liang, K., Ma, S., Huang, L., 2018. Using self-organizing map for coastal water quality classification: towards a better understanding of patterns and processes. Sci. Total Environ. 628-629, 1446–1459.
Li, Z., Zhou, X., Xu, Q., Yan, Y., He, M., Li, J., Dong, J., Tian, J., Ding, F., Li, Y., Ma, C., Wang, X., Luo, Z., 2022b. Hydrochemical characteristics of hot springs in the intersection of the Red River Fault Zone and the Xiaojiang Fault Zone, Southwest Tibet Plateau. Water 14 (16), 2525.
Liang, B., Han, G., Zeng, J., Qu, R., Liu, M., Liu, J., Zhao, Y., 2022. Zn isotope fractionation in laterites from Yunnan province, southwest China: implications for the Zn cycles and its environmental impacts in (sub-) tropics. Sci. Total Environ. 844, 157245.
Lin, S., Shen, S., Zhou, A., Lyu, H., 2021. Assessment and management of lake eutrophication: a case study in Lake Erhai, China. Sci. Total Environ. 751, 141618.
Liu, Y., Zhou, X., Deng, Z., Fang, B., Tsutomu, Y., Zhao, J., Wang, X., 2015. Hydrochemical characteristics and genesis analysis of the Jifei hot spring in Yunnan, southwestern China. Geothermics 53, 38–45.
Liu, Z., Feng, S., Zhangsong, A., Han, Y., Cao, R., 2023. Long-term evolution of groundwater hydrochemistry and its influencing factors based on self-organizing map (SOM). Ecol. Indic. 154, 110697.
Luo, Z., Zhou, X., He, M., Liang, J., Li, J., Dong, J., Tian, J., Yan, Y., Li, Y., Liu, F., Ouyang, S.P., Liu, K., Yao, B., Wang, Y., Zeng, Z., Lopez, P., 2023. Earthquakes evoked by lower crustal flow: evidence from hot spring geochemistry in Lijiang-Xiaojinhe fault. J. Hydrol. 619, 129334.
Mao, H., Wang, G., Rao, Z., Liao, F., Shi, Z., Huang, X., Chen, X., Yang, Y., 2021. Deciphering spatial pattern of groundwater chemistry and nitrogen pollution in Poyang Lake Basin (eastern China) using self-organizing map and multivariate statistics. J. Clean. Prod. 329, 129697.
McCleskey, R., Nordstrom, D., Hurwitz, S., Colman, D., Roth, D., Johnson, M., Boyd, E., 2022. The source, fate, and transport of arsenic in the Yellowstone hydrothermal system - an overview. J. Volcanol. Geotherm. Res. 432, 107709.
McLaren, S., Kim, N., 1995. Evidence for a seasonal fluctuation of arsenic in new-zealands longest river and the effect of treatment on concentrations in drinking-water. Environ. Pollut. 90 (1), 67–73.
Mia, M., Haque, M., Islam, A., Jannat, J., Jion, M., Islam, M., Siddique, M., Idris, A., Senapathi, V., Talukdar, S., Rahman, A., 2023. Analysis of self-organizing maps and explainable artificial intelligence to identify hydrochemical factors that drive drinking water quality in Haor region. Sci. Total Environ. 904, 166927.
Mohan, D., Pittman Jr., C., 2007. Arsenic removal from water/wastewater using adsorbents–a critical review. J. Hazard. Mater. 142 (1–2), 1–53.
Nguyen, T., Kawamura, A., Tong, T., Amaguchi, H., Nakagawa, N., Gilbuena, R., Bui, D., 2015. Identification of spatio-seasonal hydrogeochemical characteristics of the unconfined groundwater in the Red River Delta, Vietnam. Appl. Geochem. 63, 10–21.
Njuguna, S., Onyango, J., Githaiga, K., Gituru, R., Yan, X., 2020. Application of multivariate statistical analysis and water quality index in health risk assessment by domestic use of river water. Case study of Tana River in Kenya. Process Saf. Environ. 133, 149–158.
Ogawa, Y., Ishiyama, D., Shikazono, N., Iwane, K., Kajiwara, M., Tsuchiya, N., 2012. The role of hydrous ferric oxide precipitation in the fractionation of arsenic, gallium, and indium during the neutralization of acidic hot spring water by river water in the Tama River watershed, Japan. Geochim. Cosmochim. Ac. 86, 367–383.
Ouyang, S.P., Zhou, X., He, M., Tian, J., Li, J., Dong, J., Li, Y., Yan, Y., Liu, F., Yao, B., Wang, Y., Zeng, Z., Chen, Q., Luo, Z., Ji, G., 2023. The characteristics of the hydrogeochemical seismic anomaly of hot springs in the Ning'er-Tongguan volcanic area. J. Seismolog. Res. 46 (1), 37–48.
Peng, C., Liu, G., Liao, S., 2023. Assessment of thermal water and energy recoverable rate based on express method: a case study of Reshuiwei geothermal field. Geothermics 114, 102789.
Pinti, D., Castro, M., López-Hernández, A., Hernández-Hernández, M., Shouakar-Stash, O., Hall, C., Bahena-Romero, J., Ramírez-Montes, M., 2021. Origin of volatile species and aqueous fluids in the Los Humeros Geothermal Field, Mexico. Chem. Geol. 584, 120539.
Priya, A., Gnanasekaran, L., Dutta, K., Rajendran, S., Balakrishnan, D., Soto-Moscoso, M., 2022. Biosorption of heavy metals by microorganisms: evaluation of different underlying mechanisms. Chemosphere 307 (Pt 4), 135957.
Qu, S., Wang, G., Shi, Z., Xu, Q., Guo, Y., Ma, L., Sheng, Y., 2018. Using stable isotopes (δD,$\delta^{18}O$,$\delta^{34}S$ and $^{87}Sr/^{86}Sr$) to identify sources of water in abandoned mines in the Fengfeng coal mining district, northern China. Hydrol. J. 26 (5), 1443–1453.
Ramos, M., Yan, W., Li, X., Koel, B., Zhang, W., 2009. Simultaneous oxidation and reduction of arsenic by zero-valent iron nanoparticles: understanding the significance of the core-shell structure. J. Phys. Chem. C 113 (33), 14591–14594.
Ren, Z., Zhou, X., Yang, M., Wang, X., Zheng, Y., Li, X., Shen, Y., 2018. Hydrochemical characteristics and formation of the Madeng Hot Spring in Yunnan, China. Geofluids 2018, 1–11.
Samadi, J., 2022. Modelling hydrogeological parameters to assess groundwater pollution and vulnerability in Kashan aquifer: novel calibration-validation of multivariate statistical methods and human health risk considerations. Environ. Res. 211, 11308.
Samuel, M., Selvarajan, E., Sarswat, A., Muthukumar, H., Jacob, J., Mukesh, M., Pugazhendhi, A., 2022. Nanomaterials as adsorbents for As(III) and As(V) removal from water: a review. J. Hazard. Mater. 424 (Pt C), 127572.
Sato, T., Takahashi, H., Kawabata, K., Takahashi, M., Inamura, A., Handa, H., 2020. Changes in the nitrate concentration of spring water after the 2016 Kumamoto earthquake. J. Hydrol. 580, 124310.

Scorzini, A., Di Bacco, M., De Luca, G., Tallini, M., 2023. Deep learning for earthquake hydrology? Insights from the karst Gran Sasso aquifer in central Italy. J. Hydrol. 617, 129002.
Shen, H., Rao, W., Tan, H., Guo, H., Ta, W., Zhang, X., 2023. Controlling factors and health risks of groundwater chemistry in a typical alpine watershed based on machine learning methods. Sci. Total Environ. 854, 158737.
Shi, Z., Zhang, H., Wang, G., 2020. Groundwater trace elements change induced by M5.0 earthquake in Yunnan. J. Hydrol. 581, 124424.
Siddique, T., Dutta, N., Roy Choudhury, N., 2020. Nanofiltration for arsenic removal: challenges, recent developments, and perspectives. Nanomaterials 10 (7), 1323.
Sun, Y., Zhou, X., He, M., Yan, Y., Tian, J., Li, J., Dong, J., Zhang, Y., 2023. Geochemical characteristics and water quality assessment of trace elements in geothermal springs in the Gulu-Yadong rift, Tibetan Plateau. Geothermics 111, 102720.
Tan, H., Zhang, Y., Zhang, W., Kong, N., Zhang, Q., Huang, J., 2014. Understanding the circulation of geothermal waters in the Tibetan Plateau using oxygen and hydrogen stable isotopes. Appl. Geochem. 51, 23–32.
Tao, L., Zhu, X., Zhang, Q., Ma, Y., Wei, Z., Pang, L., Tu, C., He, C., Liu, H., 2023. Geochemical characteristics and genesis of Sr-F-Si-Rn physiotherapy hot mineral water of Reshuitang, in Gugan Town,Fuyuan County, Eastern Yunnan. Geolog. Rev. 69 (3), 959–972.
Tian, J., Pang, Z.H., Guo, Q., Wang, Y.C., Huang, T.M., Kong, Y.L., 2018. Geochemistry of geothermal fluids with implications on the sources of water and heat recharge to the Rekeng high-temperature geothermal system in the Eastern Himalayan Syntax. Geothermics 74, 92–105.
Tian, J., Zhou, X., Yan, Y., He, M., Li, J., Dong, J., Liu, F., Ouyang, S., Li, Y., Tian, L., Wang, Y., Huang, T., Pang, Z., 2023. Earthquake-induced impulsive release of water in the fractured aquifer system: insights from the long-term hydrochemical monitoring of hot springs in the Southeast Tibetan Plateau. Appl. Geochem. 148, 105553.
Tiwari, A., Suozzi, E., Fiorucci, A., Lo Russo, S., 2021. Assessment of groundwater geochemistry and human health risk of an intensively cropped alluvial plain, NW Italy. Hum. Ecol. Risk Assess. 27 (3), 825–845.
Tong, S., Li, H., Tudi, M., Yuan, X., Yang, L., 2021. Comparison of characteristics, water quality and health risk assessment of trace elements in surface water and groundwater in China. Ecotox. Environ. Safe 219, 112283.
Tong, W., Liao, Z., Liu, S., Zhang, Z., You, M., Zhang, M., 2000. Thermal Springs in Tibet. Science Press, Beijing, pp. 1–300.
Tran, T., Banning, A., Heinze, T., Wohnlich, S., 2022. Integration of self-organizing maps, statistical analysis, and hydrogeochemical modeling methods to identify spatio-seasonal variations in mine water quality. J. Geochem. Explor. 233, 106908.
Tsakovski, S., Simeonov, V., 2011. Hasse diagram technique as exploratory tool in sediment pollution assessment. J. Chemom. 25 (5), 254–261.
Vengosh, A., Helvaci, C., Karamanderesi, I., 2002. Geochemical constraints for the origin of thermal waters from western Turkey. Appl. Geochem. 17 (3), 163–183.
Wang, M., Zhou, X., Liu, Y., Xu, H., Wu, Y., Zhuo, L., 2020. Major, trace and rare earth elements geochemistry of geothermal waters from the Rehai high-temperature geothermal field in Tengchong of China. Appl. Geochem. 119, 104639.
Wang, W., Zhou, X., Shi, H., Yan, Y., Ouyang, S.P., Liu, F., Fang, W., Li, P., 2022. Hydrogeochemical characteristics of hot springs in Nantinghe fault zone, Yunnan Province. Earthquake 42 (2), 14–32.
Wang, X., Yuan, X., Shui, Q., Qi, Y., Deng, X., Yang, F., 2024. Optimized allocation of water temperature, quality, and quantity for the utilization of geothermal water from deep buried reservoirs. Geothermics 119, 102951.
Wang, Y., Cheng, H., 2023. Environmental fate and ecological impact of the potentially toxic elements from the geothermal springs. Environ. Geochem. Health 45 (8), 6287–6303.
Wei, S., Liu, F., Zhang, W., Zhang, H., Zhao, J., Liao, Y., Yan, X., 2022. Typical geothermal waters in the Ganzi–Litang fault, western Sichuan, China: hydrochemical processes and the geochemical characteristics of rare-earth elements. Environ. Earth Sci. 81 (23), 538.
Wen, B., Zhou, J., Tang, P., Jia, X., Zhou, W., Huang, J., 2023. Antimony (Sb) isotopic signature in water systems from the world's largest Sb mine, central China: novel insights to trace Sb source and mobilization. J. Hazard. Mater. 446, 130622.
Woith, H., Wang, R.J., Maiwald, U., Pekdeger, A., Zschau, J., 2013. On the origin of geochemical anomalies in groundwaters induced by the Adana 1998 earthquake. Chem. Geol. 339, 177–186.
Wu, G., Zhang, Q., Zheng, X., Mu, L., Dai, L., 2010. Water quality of Lugu Lake: changes, causes and measurements. Int. J. Sustain. Dev. World Ecol. 15 (1), 10–17.
Wu, Y., Zhou, X., Wang, M., Zhuo, L., Xu, H., Liu, Y., 2021. Comparison of hydrogeological characteristics and genesis of the Xiaguan Hot Spring and the Butterfly Spring in Yunnan of China. J. Hydrol. 593, 125922.
Xiao, J., Wang, L., Chai, N., Liu, T., Jin, Z., Rinklebe, J., 2021. Groundwater hydrochemistry, source identification and pollution assessment in intensive industrial areas, eastern Chinese loess plateau. Environ. Pollut. 278, 116930.
Xie, X., Zhang, M., Liu, W., Liu, Y., Lang, Y., Xu, S., 2024. Active CO_2 emissions from thermal springs in the Karakoram fault system and adjacent regions, western Tibetan Plateau. Appl. Geochem. 161, 105896.
Yan, Y., Zhang, Z., Zhou, X., Wang, G., He, M., Tian, J., Dong, J., Li, J., Bai, Y., Zeng, Z., Wang, Y., Yao, B., Xing, G., Cui, S., Shi, Z., 2024. Geochemical characteristics of hot springs in active fault zones within the northern Sichuan-Yunnan block: geochemical evidence for tectonic activity. J. Hydrol. 635, 131179.
Yang, S., Liang, R., Chen, J., Wang, Y., Li, K., 2024. Estimating the water quality index based on interpretable machine learning models. Water Sci. Technol. 89 (5), 1340–1356.
Yang, X., Jia, C., Yang, F., Yang, H., Yao, Y., 2023. Spatio-temporal variation of groundwater pollution in urban wetlands and management strategies for zoning. J. Environ. Manage. 342, 118318.
Yotova, G., Varbanov, M., Tcherkezova, E., Tsakovski, S., 2021. Water quality assessment of a river catchment by the composite water quality index and self-organizing maps. Ecol. Indic. 120, 106872.
Zhang, B., Song, X., Zhang, Y., Han, D., Tang, C., Yu, Y., Ma, Y., 2012. Hydrochemical characteristics and water quality assessment of surface water and groundwater in Songnen plain, Northeast China. Water Res. 46 (8), 2737–2748.
Zhang, G., Liu, C.Q., Liu, H., Jin, Z., Han, G., Li, L., 2008. Geochemistry of the Rehai and Ruidian geothermal waters, Yunnan Province, China. Geothermics 37 (1), 73–83.
Zhang, H., 2022. Study On Temporal and Spatial Variation of Water Resources Carrying Capacity in Yunnan Province [Doctoral]. China University of Geosciences, Beijing.
Zhang, L., Guo, L., Wang, Y., Liu, D., Liu, Y., Li, J., 2020a. Continuous monitoring of hydrogen and oxygen stable isotopes in a hot spring: significance for distant earthquakes. Appl. Geochem. 112, 104488.
Zhang, L., Liang, X., Xiao, C., Yang, W., Zhang, J., Wang, X., 2023. Hydrochemical characteristics and the impact of human activities on groundwater in a semi-arid plain: a case study of western Jilin Province, Northeast China. Environ. Sci. Pollut 30 (51), 110204–110219.
Zhang, Y., Tan, H., Zhang, W., Wei, H., Dong, T., 2016. Geochemical constraint on origin and evolution of solutes in geothermal springs in western Yunnan, China. Geochemistry 76 (1), 63–75.
Zhang, Y., Xu, M., Li, X., Qi, J., Zhang, Q., Guo, J., Yu, L., Zhao, R., 2018. Hydrochemical characteristics and multivariate statistical analysis of natural water system: a case study in Kangding County, Southwestern China. Water 10 (1), 80.
Zhang, Y., Yan, Y.T., Yao, R.W., Wei, D.H., Huang, X., Luo, M., Wei, C.L., Chen, S., Yang, C., 2024. Natural background levels, source apportionment and health risks of potentially toxic elements in groundwater of highly urbanized area. Sci. Total Environ. 935, 173276.
Zhang, X., Zhao, R., Wu, X., Mu, W., Wu, C., 2022. Delineating the controlling mechanisms of arsenic release into groundwater and its associated health risks in the Southern Loess Plateau, China. Water Res. 219, 118530.
Zhang, Y., Zhou, X., Liu, H., Fang, B., 2020b. Geochemistry of rare earth elements in the hot springs in the Simao Basin in southwestern China. Environ. Earth Sci. 79 (6).
Zhang, Z., Zhang, W., Hu, X., Li, K., Luo, P., Li, X., Xu, W., Li, S., Duan, C., 2020c. Evaluating the efficacy of point-of-use water treatment systems using the water Quality index in rural Southwest China. Water 12 (3), 121.
Zhong, C., Wang, H., Yang, Q., 2022. Hydrochemical interpretation of groundwater in Yinchuan basin using self-organizing maps and hierarchical clustering. Chemosphere 309, 136787.
Zhou, H., Zhou, X., Su, H., Li, Y., Liu, F., Ouyang, S., Yan, Y., Bai, R., 2022. Hydrochemical characteristics of earthquake-related thermal springs along the Weixi–Qiaohou Fault, Southeast Tibet Plateau. Water 14 (1), 132.
Zhou, L., Ye, T., Zheng, S., Zhu, X., Chen, Z., Wu, Y., 2023a. Experimental and modeling investigation of dual-source iron release in water-solid-gas interaction of abandoned coal mine drainage. Environ. Geochem. Health 45 (11), 8433–8449.
Zhou, R., Zhou, X., He, M., Tian, J., Zhang, Y., Dong, J., Li, J., Zhao, Q., 2024. Fluid geochemical characteristics of Hot springs in Eastern Yunnan. Bull. Mineral. Petrol. Geochem. Accepted.
Zhou, X., Zhuo, L., Wu, Y., Tao, G., Ma, J., Jiang, Z., Sui, L., Wang, Y., Wang, C., Cui, J., 2023b. Origin of some hot springs as conceptual geothermal models. J. Hydrol. 624, 129927.
Zhu, G., Wu, X., Ge, J., Liu, F., Zhao, W., Wu, C., 2020. Influence of mining activities on groundwater hydrochemistry and heavy metal migration using a self-organizing map (SOM). J. Clean. Prod. 257, 120664.
Zhuang, S., Wang, G., Zhou, X., Shi, Z., Yuan, D., Tian, J., He, M., Zeng, Z., Yan, Y., Yao, B., Wang, Y., Xing, G., Cui, S., 2024. Deciphering the distribution and enrichment of arsenic in geothermal water in the Red River Fault Zone, southwest China. J. Hazard. Mater. 485, 136756.